

# First survey of Wolf-Rayet star populations over the full extension of nearby galaxies observed with CALIFA<sup>★</sup>

D. Miralles-Caballero<sup>1\*\*</sup>, A. I. Díaz<sup>1</sup>, Á. R. López-Sánchez<sup>2,3</sup>, F. F. Rosales-Ortega<sup>4</sup>, A. Monreal-Ibero<sup>5</sup>, E. Pérez-Montero<sup>6</sup>, C. Kehrig<sup>6</sup>, R. García-Benito<sup>6</sup>, S. F. Sánchez<sup>7,6</sup>, C. J. Walcher<sup>8</sup>, L. Galbany<sup>9,10</sup>, J. Iglesias-Páramo<sup>6</sup>, J. M. Vílchez<sup>6</sup>, R. M. González Delgado<sup>6</sup>, G. van de Ven<sup>11</sup>, J. Barrera-Ballesteros<sup>12</sup>, M. Lyubenova<sup>11</sup>, S. Meidt<sup>13</sup>, J. Falcon-Barroso<sup>12</sup>, D. Mast<sup>14,6</sup>, M. A. Mendoza<sup>6</sup>, and the CALIFA collaboration.

(Affiliations can be found after the references)

May 16, 2016

## ABSTRACT

The search of extragalactic regions with conspicuous presence of Wolf-Rayet (WR) stars outside the Local Group is challenging task due to the difficulties in detecting their faint spectral features. In this exploratory work, we develop a methodology to perform an automated search of WR signatures through a pixel-by-pixel analysis of integral field spectroscopy (IFS) data belonging to the *Calar Alto Legacy Integral Field Area* survey, CALIFA. This procedure has been applied to a sample of nearby galaxies spanning a wide range of physical, morphological and environmental properties. This technique allowed us to build the first catalogue of Wolf-Rayet rich regions with spatially-resolved information, allowing to study the properties of these complexes in a 2D context. The detection technique is based on the identification of the blue WR bump (around He II  $\lambda 4686$  Å, mainly associated to nitrogen-rich WR stars, WN) and the red WR bump (around C IV  $\lambda 5808$  Å and associated to carbon-rich WR stars, WC) using a pixel-by-pixel analysis, which maximizes the number of independent regions within a given galaxy. We identified 44 WR-rich regions with blue bumps distributed in 25 galaxies of a total of 558. The red WR bump was identified only in 5 of those regions. Most of the WR regions are located within one effective radius from the galaxy centre, and around 1/3 are located within  $\sim 1$  kpc or less from the centre. We found that the majority of the galaxies hosting WR populations in our sample are involved in some kind of interaction process. Half of the host galaxies share some properties with gamma-ray burst (GRB) hosts where WR stars, as potential candidates to being the progenitors of GRBs, are found. We also compared the WR properties derived from the CALIFA data with stellar population synthesis models, and confirm that simple star models are generally not able to reproduce the observations. We conclude that other effects, such as the binary star channel (which could extend the WR phase up to 10 Myr), fast rotation or other physical processes that causes the loss of observed Lyman continuum photons, are very likely affecting the derived WR properties, and hence should be considered when modelling the evolution of massive stars.

**Key words.** galaxies: starburst – galaxies: ISM – stars: Wolf-Rayet – techniques: imaging spectroscopy

## 1. Introduction

Despite their relatively low number, massive stars dominate the stellar feedback to the local interstellar medium (ISM) through their stellar winds and subsequent death as supernovae (SNe). The most massive stars ( $M \geq 25 M_{\odot}$  for  $Z_{\odot}$ ) will undergo the Wolf-Rayet (WR) phase, starting 2–3 Myr after their birth (Meynet 1995). These stars have typical wind densities which are an order of magnitude higher than massive O stars, and hence play a key role to the chemical enrichment of galaxies. Although evading direct detection, WR stars are likely to be the progenitors of Type Ib and Type Ic core-collapse SNe, likely linked to the on-going star-formation (Galbany et al. 2014). These SN types are characterised by neither showing Hydrogen (SNIb) nor Helium (SNIc) in their spectra, suggesting that the external layers of the progenitor star have been removed prior to explosion. Moreover, a small

fraction of SNe Ic showing broad-line features in the spectra (SNIc-bl,  $\sim 30,000 \text{ km s}^{-1}$ ) are associated to long-duration gamma-ray bursts (GRBs, Galama et al. 1998; Stanek et al. 2003; Hjorth et al. 2003; Modjaz et al. 2006). Indeed, WR stars have been suggested to be candidates to being progenitors of long, soft GRBs in regions of low metallicity (Woosley & Heger 2006).

The emission features that characterize the spectra of WR stars are often observed in extragalactic H II regions. WR winds are sufficiently dense that an optical depth of unity in the continuum arises in the outflowing material. The spectral features are formed far out in the wind and are seen primarily in emission (Crowther 2007). Generally WR stars are identified in galaxies (first renamed as “WR galaxies” by Osterbrock & Cohen 1982) whenever their integrated spectra show a broad He II emission feature centred at  $4686 \text{ Å}$ , the so-called blue WR bump. Some few other broad features, as the red WR bump around C IV  $\lambda 5808$ , are also used to identify WR stars in galaxies, but these features are in most cases much fainter than the blue WR bump. In any case, it is important to note that the term “WR galaxy” may be confusing. Depending on the distance to the observed galaxy and the spatial resolution

<sup>★</sup> Based on observations collected at the Centro Astronómico Hispano-Alemán (CAHA) at Calar Alto, operated jointly by the Max-Planck Institut für Astronomie and the Instituto de Astrofísica de Andalucía (CSIC).

<sup>\*\*</sup> e-mail: thorius@gmail.com

and extension of the extracted spectrum, it may well refer to extragalactic H II regions and quite frequently to the nucleus of a powerful starburst. Galaxies showing a significant population of WR stars have been known for several decades, beginning with the first WR detection in the blue compact dwarf galaxy He 2-10 (Allen et al. 1976). Since then a number of the WR galaxies have been reported, though generally through a serendipitous detection (e.g. Kunth & Sargent 1981, 1983; Ho et al. 1995; Heckman et al. 1997).

The investigation of the WR content in galaxies provides important constraints to stellar evolutionary models. This is particularly important at low metallicities because only few data of sub-solar WR stars are available. Several studies have attempted to reproduce the number of WR stars needed to account for the observed stellar emission features. The disagreement between observations and models on simple calculations, such as the flux ratio between the blue WR bump and H $\beta$  or the WR/O number ratio at sub-solar metallicities (which is a sensitive test of evolutionary models), has led to the development of sophisticated models which include rotation (Meynet & Maeder 2005) or binary evolution of massive stars (Van Bever & Vanbeveren 2003; van Bever & Vanbeveren 2007; Eldridge et al. 2008). Therefore, studies of large samples of galaxies showing WR features, especially in the intermediate- and low-metallicity regime, are needed to better constrain such models.

Ideally, detailed, spatially-resolved studies of WR populations would be needed to fill the gap between early detailed works and large surveys of integrated properties. Several studies in nearby starbursts (e.g. Gonzalez-Delgado et al. 1994; Pérez-Montero & Díaz 2007; Pérez-Montero et al. 2010; López-Sánchez & Esteban 2010; Karthick et al. 2014) and resolved knots of star formation (e.g. Gonzalez-Delgado et al. 1995; Castellanos et al. 2002; Hadfield & Crowther 2006) have been published during the last few years, in conjunction with studies of individual WR stars in galaxies of the Local Group (e.g. Massey & Hunter 1998; Massey 2003; Crowther & Hadfield 2006; Crowther et al. 2006; Neugent et al. 2012; Hainich et al. 2014; Sander et al. 2014). However, spatially-resolved and detailed studies of extragalactic regions showing a significant WR population in large galaxy samples have not been accomplished yet.

The advent of the integral field spectroscopy (IFS) allows to obtain simultaneously both spectral and spatial information of galaxies. Therefore, IFS techniques provide a more efficient way to study the spatial distribution of the WR population in nearby galaxies. Indeed, such studies have been conducted in some individual galaxies (e.g. James et al. 2009; López-Sánchez et al. 2011; Monreal-Ibero et al. 2013; Kehrig et al. 2013). In particular, Miralles-Caballero et al. (2014b) (henceforth, MC14b) used data from the PPAK Integral Field Spectroscopy (IFS) Nearby Galaxies Survey (PINGS Rosales-Ortega et al. 2010) to locate the WR-rich regions in the nearby spiral galaxy NGC 3310. PINGS was specifically designed to study the spatially-resolved properties of a sample of 17 nearby spiral galaxies. Among the almost 100 H II regions identified throughout the disc of NGC 3310 by Miralles-Caballero et al. (2014a), MC14b reported the detection of WR features in 18 of them. The methodology developed by MC14b using IFS data mitigates aperture effects and allows to spatially resolve the emission of the WR population in local galaxies (Kehrig et al. 2013). Indeed, their technique can be applied to large galaxy samples. IFS observations also provide powerful tools to minimize the WR bump dilution and find WR stars in

extragalactic H II regions where they were not detected before (Kehrig et al. 2008; Cairós et al. 2010; García-Benito et al. 2010; Monreal-Ibero et al. 2010, 2012; Pérez-Montero et al. 2013). In addition, spatially resolved studies can also be used to explore the connection between the environment and the WR emission. The study of the environment is of particular interest to get clues about the connection between WR stars and SNIc-bl/GRBs, since these massive stars may actually be progenitors of these explosions. Although a direct link between GRBs to WR stars cannot be made, it is possible to compare the properties of GRB host galaxies with those of WR stars and indirectly obtain information on the GRB progenitors in this way. Kelly et al. (2008), expanding the work by Fruchter et al. (2006), showed that both SNIc-bl and GRB tend to occur in the brightest regions of their host galaxies. Leloudas et al. (2010) correlated the locations of WR stars with GRBs and different SN types finding that SNe Ibc and WR showed a high degree of association, and that the connection between WR and GRBs could not be excluded. Some other studies have reported that the host galaxies of nearby GRB often host WR stars too, although the WR-rich areas do not necessarily coincide with the location of the GRBs (Cerviño 1998; Hammer et al. 2006; Christensen et al. 2008; Han et al. 2010; Levesque et al. 2011; Thöne et al. 2014). Therefore, studies of WR galaxies and their relation with their environment may also provide insight into the properties of GRB progenitors.

Previous searches for WR regions across individual galaxies outside the Local Group have been performed, for example in NGC 300 (Schild et al. 2003), M83 (Hadfield et al. 2005), NGC 1313 (Hadfield & Crowther 2007), NGC 7793 (Bibby & Crowther 2010), NGC 5068 (Bibby & Crowther 2012), and M101 (Shara et al. 2013). Nowadays a systematic search for the spatially resolved WR populations in sample of nearby galaxies can be performed with the aid of IFS. Examples include Brinchmann et al. (2008a) (henceforth B08a), but also Shirazi & Brinchmann (2012) who accomplished the task by analysing a few hundred thousand spectra obtained with fibres. In this work we analyse a sample of 558 galaxies observed with IFS to compile for the first time a homogeneous catalogue of galaxies showing regions with WR populations. Galaxies of all different environments were considered, i.e. isolated galaxies, compact dwarf galaxies, as well as targets showing past signs of recent and ongoing interactions. Thanks to the 2D coverage of IFS data we were able to identify resolved H $\alpha$  clumps in the galaxies, thus avoiding restricting the search of WR-rich areas to only the brightest H II complexes, as it is usually imposed in other studies. The main goal of this article is to relate for the first time the WR populations in this homogeneous galaxies sample with their spatially resolved properties, to explore the influence of morphology in the recurrence of these features, and to study the effect of binarity, photon leakage and metallicity in the observed properties of WR emission lines in the Local Universe.

The paper is organized as follows: Sec. 2 presents our IFS galaxy sample and gives some details about the data reduction process. We then describe the methodology used to pinpoint regions showing WR emission using data from IFS surveys in Sec. 3. Sec. 4 presents our catalogue of regions showing WR emission features. Here we outline the overall properties of the host galaxies and describe the procedure to measure the different components of the WR features. These measurements are later used to estimate the number of WR stars in each region. In Sec. 5 we discuss the influence of the environment and the GRB-WR connection, quantifying the effect of the dilution of

the WR features when integrating over larger apertures than the observed spatial extent of the WR population, and comparing our observations with the predictions provided by synthesis stellar models. Finally, we present our conclusions in Sec. 6.

## 2. Initial sample and data reduction

The galaxies of this study were mainly selected from the Calar Alto Legacy Integral Field Area: CALIFA survey (Sánchez et al. 2012a), an ongoing exploration of the spatially resolved spectroscopic properties of galaxies in the Local Universe ( $z < 0.03$ ) using wide-field IFS. CALIFA observations cover the full optical extent (up to  $\sim 3 - 4$  effective radii) of around 600 galaxies of any morphological type, distributed across the entire colour-magnitude diagram Walcher et al. (2014). Observations were carried out using the Potsdam MultiAperture Spectrophotometer (Roth et al. 2005), mounted at the Calar Alto 3.5m telescope, in the PPAK configuration (Kelz et al. 2006). The observations cover a hexagonal field-of-view (FoV) of  $74'' \times 64''$ , which allows to map the full optical extent of the galaxies up to two to three effective radii. A dithering scheme of three pointings was adopted in order to cover the complete FoV and properly sample the PSF. The observing details, selection of the galaxy sample, observational strategy, and reduction processes are thoroughly explained in Sánchez et al. (2012a) and Walcher et al. (2014). CALIFA has recently launched to the astronomical community its second data release DR2<sup>1</sup>, a set of fully reduced, quality tested and scientifically useful data cubes for 200 galaxies (García-Benito et al. 2014).

For the purpose of our study, we used 448 galaxies from the CALIFA survey observed by April 2014 in the V500 spectral set-up, that has a nominal resolution of  $\lambda/\Delta\lambda \sim 850$  at 5000 Å and a nominal wavelength range of 3749–7300 Å. The dataset was reduced using the version 1.5 of the CALIFA pipeline (García-Benito et al. 2014). The usual reduction tasks per pointing include cosmic rays rejection, optimal extraction, flexure correction, wavelength and flux calibration, and sky subtraction. Finally, all three pointings are combined to reconstruct a spatially  $1'' \times 1''$  re-sampled data cube, that includes science data, propagated error vectors, masks and weighting factors (see Sánchez et al. 2012a and Husemann et al. 2013 for more details). The average value of the PSF of the datacubes is around  $2.5''$  (García-Benito et al. 2014). In addition, 110 galaxies from the “CALIFA-Extension” programs were also included as part of our data. The CALIFA-Extension sample consist of galaxies not included in the main CALIFA sample that are part of specific science programs using the same observing set-up as CALIFA. This sample includes interactive, merging and low-mass galaxies (classes S0, Sb and dwarfs), providing a complementary to main sample since CALIFA becomes incomplete below  $M_r > -19$  mag (which corresponds to a stellar mass of  $\sim 10^{9.5} M_\odot$ ).

With a redshift range of  $0.005 < z < 0.03$  and absolute magnitudes above  $M_z = -16$ , the sample is representative of the galaxy population in the Local Universe (Walcher et al. 2014). Note that this sample is not purposely selected to detect as many WR features as possible, given that these populations can only be found when young ionising stellar populations exist (i.e., typically within the first million years after they are born). Yet, this is up to now the largest sample of galaxies observed using a wide field-of-view ( $> 1$  arcmin<sup>2</sup>) IFS. It contains hundreds

of star-forming objects (including spiral, barred, irregular and merging galaxies as well as blue compact dwarfs), and it is expected to host a significant number of regions where populations of WR stars can be detected. With these data we can resolve regions larger than about 100 pc in radius in the closest galaxies and larger than about 600 pc in the furthest systems. These sizes are typical for giant extragalactic H II regions and H II complexes (Kennicutt 1984; González Delgado & Pérez 1997; Youngblood & Hunter 1999; Hunt & Hirashita 2009; Lopez et al. 2011; Miralles-Caballero et al. 2011).

## 3. Identification of WR features in IFS surveys

WR stars have been typically discovered via techniques sensitive to their unusually broad emission-line spectra. As mentioned before, the most prominent WR emission feature observed in optical spectra corresponds to the so-called blue bump, a blend of a broad He II line at 4686 Å, nitrogen and carbon emission lines formed in the expanding atmospheres of the WR stars, and several high-excitation emission lines (sometimes including a narrow He II line) covering the spectral range 4600–4700 Å (Schaerer & Vacca 1998). The blue WR bump, however, is generally very faint, its flux being usually only a few percent of the flux of the H $\beta$  emission line. The red WR bump centred around 5808 Å, is usually even fainter than the blue WR bump. Therefore, a systematic search for signatures of WR emission is intrinsically challenging.

Early studies relied on the use of imaging with a narrow-band  $\lambda 4686$  filter to detect, with great effort, the spatially-resolved emission of several WRs in very nearby low-mass galaxies (Drissen et al. 1990; Sargent & Filippenko 1991; Drissen et al. 1993a,b). Very detailed studies, in most cases even for individual stars, have been accomplished using the catalogues reported in these studies (e.g. Abbott et al. 2004; Drissen et al. 2008; Úbeda & Drissen 2009). At farther distances, faint WR signatures can be detected via the analysis of integrated spectra obtained using optical fibres or long slits (e.g. Kunth & Joubert 1985; Vacca & Conti 1992; Izotov et al. 1997). These studies allowed the compilation of a few catalogues of 40–140 WR galaxies (Conti 1991; Schaerer et al. 1999; Guseva et al. 2000). The most recent surveys of WR galaxies have used single-fibre spectra from the Sloan Digital Sky Survey (SDSS<sup>2</sup>). The catalogue compiled by B08a reported 570 new WR galaxies using SDSS, and Shirazi & Brinchmann (2012) added later 189 new WR galaxies. However, these catalogues are limited to the size of the fibre ( $3''$ ), and hence they are not able to spatially resolve the WR population. Besides, galaxies observed by SDSS show a very broad distribution of distances, sampling very heterogeneous sizes and apertures. For this study, we first focused the effort on the detection of the blue bump in our search for WR spectral signatures. Once we developed the technique we did use it to detect the red bump, as explained below.

### 3.1. Identification of regions with the blue WR bump

Since only very massive stars ( $M_{\text{ini}} > 25 M_\odot$  for  $Z_\odot$ ) undergo the WR phase, typically 2 – 3 Myr after their birth (Meynet 1995), the first natural place to search for the WR emission is where the H II regions are located. However, given that most of the stars in a cluster will not undergo this phase, the location of the WR stars can be restricted to a fraction of the total area of the H II region,

<sup>1</sup> [http://www.caha.es/CALIFA/public\\_html/?q=content/califa-2nd-data-release](http://www.caha.es/CALIFA/public_html/?q=content/califa-2nd-data-release)

<sup>2</sup> <http://www.sdss.org/>



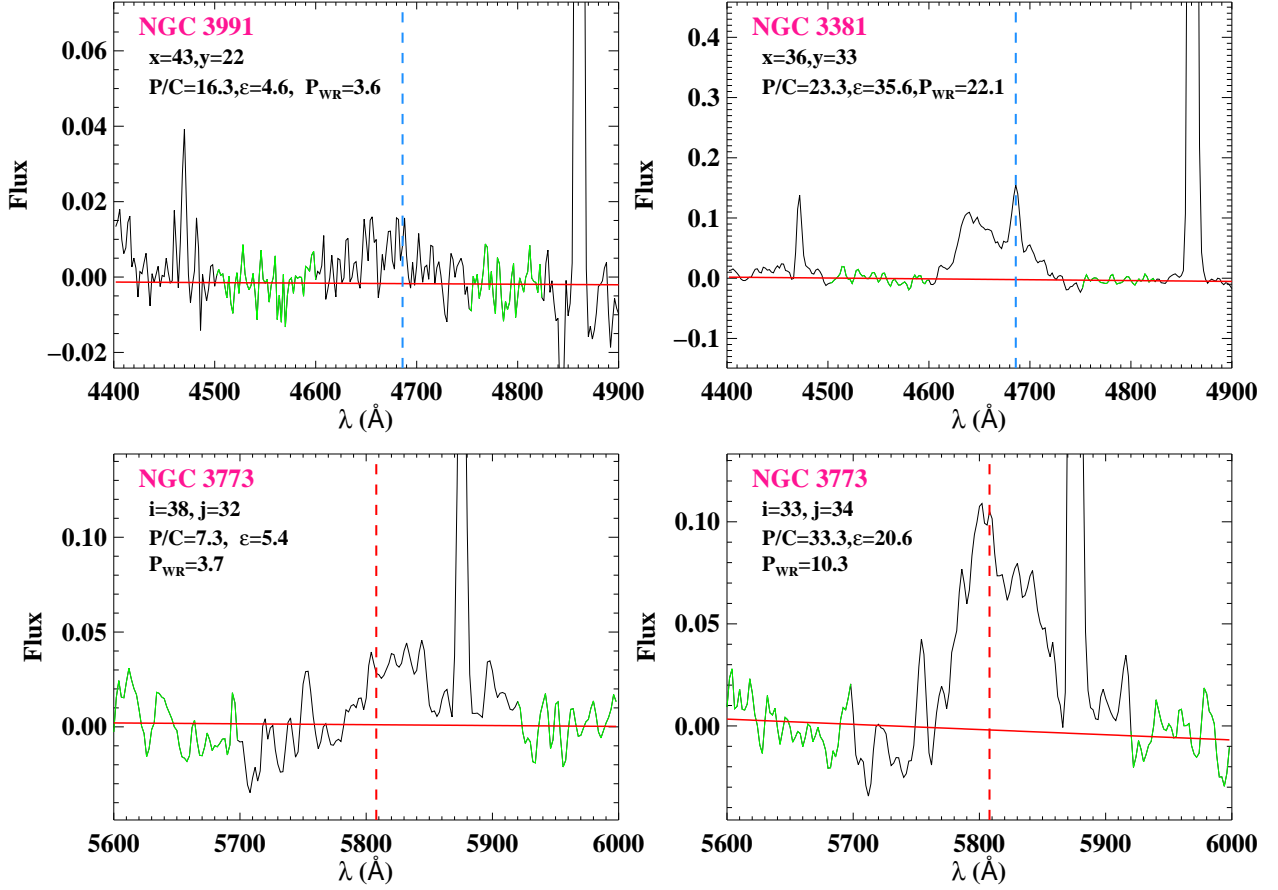


**Fig. 1: Top:** Examples of continuum-subtracted spectra for a given pixel in NGC 3991 and NGC 3381 around the blue WR bump spectral range. The blue vertical line shows the location of the He II  $\lambda 4686$  emission line. The spatial coordinates of the pixels ( $x$  and  $y$ ) and the  $P/C$ ,  $\epsilon$ , and  $P_{WR}$  parameters defined in the text are given on the left-top corner of each panel. A red continuous line indicates a linear fit to the continuum (which ideally should be an horizontal line at  $y=0$ ). The green sections of the spectrum correspond to those spectral ranges used to compute the *rms*. **Bottom:** Examples of continuum-subtracted spectra for a given pixel in NGC 3773 around the red WR bump spectral range. The red vertical line indicates the location of the C IV  $\lambda 5808$  emission line. The coordinates of the pixels and their associated parameters are also given on the left-top corner. In both the blue and the red WR bump cases one spectrum at the limit of the detection level (left) and another with a very good detection level (right) are shown. The flux density is given in units of  $10^{-16} \text{ erg s}^{-1} \text{ cm}^{-2} \text{ \AA}^{-1}$ .

this effect was noticed by Kehrig et al. (2013) (see Fig. 5 and 6). Thus the reason why our approach relies on performing a pixel-by-pixel analysis of the spectra<sup>3</sup>. The procedure followed to detect WR signatures in our galaxy sample is described as follows:

1. The first step consists in subtracting the underlying stellar population using the STARLIGHT code (Cid Fernandes et al. 2004, 2005) in order to better characterize the continuum and therefore better observe the faint WR features. It is important to note that by construction, the subtraction of the underlying continuum refers to the large scale galaxy stellar content, not including young stars cluster populations and their likely emission. A reduced spectral library set of 18 populations (3, 63, 400, 750, 2000 and 12000 Myr, combined with  $Z_{\odot}$ ,  $Z_{\odot}/2.5$  and  $Z_{\odot}/5$  metallicities) is used, so as to deal with the large amount of pixels that had to be

analysed in a reasonable amount of time. These models were selected from the compilation by González Delgado et al. (2005) and the MILES library (Vazdekis et al. 2010, as updated by Falcón-Barroso et al. 2011).

2. As only massive, young ionising stars are able to undergo the WR phase, we focused only in those pixels whose approximate  $H\alpha$  equivalent width,  $EW(H\alpha)$ , is of the order of 6 Å or higher (Cid Fernandes et al. 2011; Sánchez et al. 2014). Given that the widths of the nebular lines are rather similar for the whole sample ( $\sigma \sim 2.8$  Å, with no presence of emission from an AGN or other broader components), and assuming a Gaussian fit, we can roughly estimate  $EW(H\alpha)$  just by measuring the observed peak of the  $H\alpha$  emission over the continuum ( $\equiv P/C$ ). Under these assumptions,  $P/C > 0.85$  practically ensures that we are dealing with a young ionising population.
3. Next, using a similar approach to that discussed in B08a, which simulates early studies that used narrow band images (e.g. Drissen et al. 1990; Sargent & Filippenko 1991; Drissen et al. 1993a,b), we define a pseudo-filter spanning

<sup>3</sup> Note that the spatial element with an independent spectrum is usually called *spaxel* in IFS, in this work we will use pixel and spaxel indistinctly.

the 4600-4700 Å rest-frame range. For each pixel, we integrate the density flux,  $F_{\text{bump}}$ , within this spectral range and compare it with the  $rms$  in two spectral windows, 4500-4600 Å and 4750-4825 Å. We then define the detection significance,  $\varepsilon$ , as (Tresse et al. 1999):

$$\varepsilon = \frac{F_{\text{bump}}}{\sigma} = \frac{F_{\text{bump}}}{\sigma_c D \sqrt{2N + \frac{EW}{D}}} \approx \frac{F_{\text{bump}}}{\sigma_c D \sqrt{2N}} \quad (1)$$

where  $\sigma_c$  is the mean standard deviation per spectral point on the continuum on each side of the bump feature,  $D$  denotes the spectral dispersion in Å per spectral point,  $N$  corresponds to the number of spectral points used in the integration of the flux density and  $EW$  refers to the equivalent width of the bump. Since  $EW$ s as low as just a few Å are expected, we neglect its contribution in the equation. After performing several visual inspections we set the procedure to select only those spaxels with  $\varepsilon > 4$ .

4. WR features are broad and have different shapes, as the velocity structure of the WR winds changes between different WR stars, varying significantly the appearance of the features. The best approach to build up a reliable technique to detect WR features therefore is to construct a training set where WR features are clearly visible and the numerical values of detection parameters can be tested. We constructed such a training set by visual inspection of a set of spectra with tentative detections. We used the parameter  $P_{\text{WR}}$ , which is the peak value within the WR filter range normalized to the  $rms$ . We select those pixels with  $P_{\text{WR}} \equiv \frac{\text{Peak}}{\sigma_c} > 3.5$ . In a few cases, practically a pure narrow emission (i.e., with a width similar to that of  $H\beta$ ) is observed, identified as a narrow  $\text{He II } \lambda 4686$  emission line. It is still not clear if this narrow feature is intimately linked with the appearance of hot WR stars (Schaerer & Vacca 1998; Crowther & Hadfield 2006) or to O stars at low metallicities (Kudritzki 2002). We thus additionally impose  $\frac{\varepsilon}{P_{\text{WR}}} > 1.1$  to avoid such cases.
5. Finally, a plausible detection should occupy an area similar or larger than the CALIFA PSF. Therefore, we imposed a minimum of 9 adjacent spatial elements satisfying the previous criteria to declare a positive detection. This corresponds roughly to the size of the PPAK PSF according to García-Benito et al. (2014).

Fig. 1 (top) shows two examples to illustrate how our procedure works. As can be observed, it is not difficult to obtain positive detections with low significance levels when using the adopted criteria. Based on our training sample, whenever there is WR emission,  $\varepsilon$  peaks in a pixel and then decreases radially down to the levels of the cuts we have used. The criterion of gathering at least 9 grouped pixels helps to reject individual pixels with low significance levels.

### 3.2. Identification of regions with red WR bump

The detection of the red WR bump was made using a similar procedure than the one explained for detecting the blue WR bump. In this case, the continuum windows at each side of the bump are 5600-5700 Å and 5920-6000 Å, the latter window was chosen to avoid the bright  $\text{He I } 5876$  Å emission line. Since the red WR bump is generally fainter than the blue WR bump and very close to the  $\text{He I}$  line, their detection is more challenging

that searching for the blue WR bump, so we increased the significance level to  $\varepsilon_{\text{red}} > 5$  to select those pixels with positive detections.

Fig. 1 (bottom) shows two examples to illustrate how the procedure of searching for the red WR bump works. Now the continuum is noisier than that for the blue WR bump, and even some structure is also observed. Besides, the tail of the red WR bump coincides with the  $\text{He I}$  line at 5876 Å.

### 3.3. Constraining the search of WR features

Using the selection criteria described above on every individual pixel, a positive detection of WR features in several thousands of pixels was obtained, for all values of the considered P/C range (see Fig. 2, left). We define this as our “pre-selected sample”. However, after applying criterion 5, the number of pixels with a positive detection reduced dramatically, to several hundreds. We define this as our “selected sample”. It is interesting to note that the majority of the pixels in this restricted sample have P/C values higher than 2.1 (Fig. 2, middle), which corresponds to  $EW(H\alpha) \sim 15$  Å. This is not a very high value, since for simple (not binary) population models the WR phase normally ends 5–6 Myr after the stars are born and this  $EW$  value clearly indicates a dominant stellar population older than that. For reference, according to POPSTAR models (Mollá et al. 2009; Martín-Manjón et al. 2010) at solar metallicity,  $EW(H\alpha)$  is of the order of 15 Å for a starburst with an age  $\tau \sim 8.3$  Myr. But we have to take into account that the measured  $EW$ s may well be reduced by the continuum of non-ionising stellar populations. All in all, at the depth and spatial resolution of the data used in this study, a lower limit for the  $EW(H\alpha)$  can be considered as a safe value to look for WR emission features in galaxies in the Local Universe. Had we placed the cut of the P/C parameter at 2.1, we would have analysed less than half the initial pixel sample.

By inspection of Fig. 2 (right) the histogram of  $\varepsilon$  for the different samples of pixels (black histogram, initial sample with  $P/C > 0.85$ ; red histogram, the pre-selected sample; and finally, green histogram, the selected sample) we observe that the initial sample behaves well following a Gaussian function, centred at zero and with a width of 2.5. This is the expected behaviour of a random distribution centred at zero, i.e., with no detection at all. However, a tail appears in the distribution for  $\varepsilon > 6$ . Therefore, the pixels in the selected sample are statistically discriminated against those following a random distribution, strengthening the validity of the detection. It is also worth noting that below  $\varepsilon = 8$  the dotted distribution (pixels from the pre-selected sample excluding those from the selected sample) exceeds significantly the green distribution, which means that below this value it is hard to distinguish between real positive detections and noise. That is the main reason why the additional grouping criterion was introduced. In contrast, when  $\varepsilon > 10$  the green distribution clearly dominates over the dotted one, indicating that when a detection is made in a pixel at this significance level it will very likely represent a position with a resolved region with real WR features.

Regarding the red WR bump, it was only detected at high P/C (Fig. 3). The lowest value of this parameter for pixels with positive detection of this bump is  $P/C \sim 9$ , which corresponds to  $EW(H\alpha) \sim 60$  Å. This gives us an explanation of why it is generally more difficult to observe the red WR bump than the blue bump. The former is weaker than the latter and the presence of underlying non-ionising stellar population dilutes it

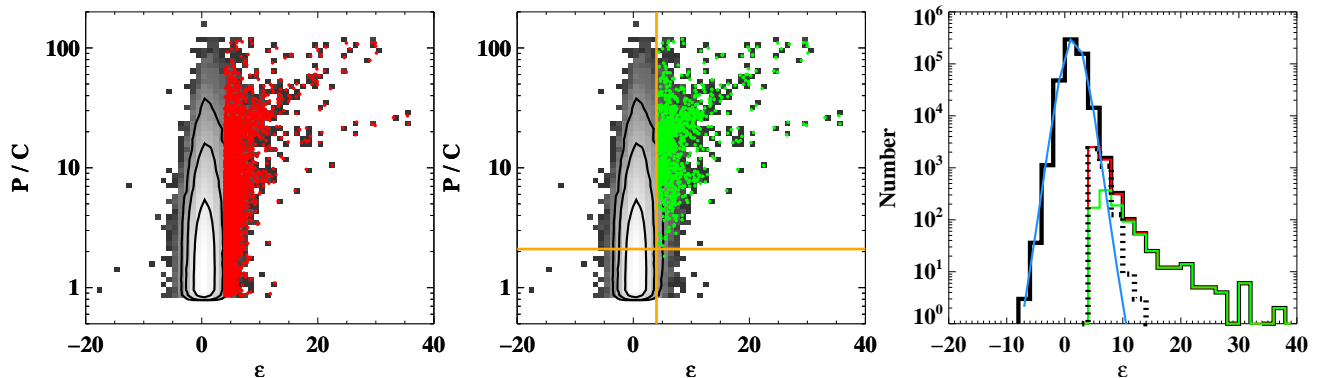


**Fig. 2:** **Left:** Density plot (grey scale) of  $P/C$  vs.  $\varepsilon$  parameters for all the pixels in the sample for which  $P/C > 0.85$ . Contours that contain 68% ( $1\sigma$ ), 95% ( $2\sigma$ ) and 99% ( $3\sigma$ ) of the points are overplotted. Red dots correspond to the values of the pre-selected regions, i.e., before imposing the grouping of at least 9 pixels. **Middle:** Same as before, but this time the overplotted green dots correspond to selected regions, obeying also the grouping criterion. The orange vertical line indicates the cut used for  $\varepsilon$  (4), while the horizontal line denotes  $P/C \sim 2.1$  parameter, having practically all the selected pixels a higher value than this limit. **Right:** Histogram of  $\varepsilon$  for pixels with  $P/C > 0.85$  (black), pre-selected pixels (red), selected pixels (green) and for those pre-selected pixels not satisfying the grouping criterion (dotted black). The curve resulting from a Gaussian fit of the black histogram is overplotted in blue.

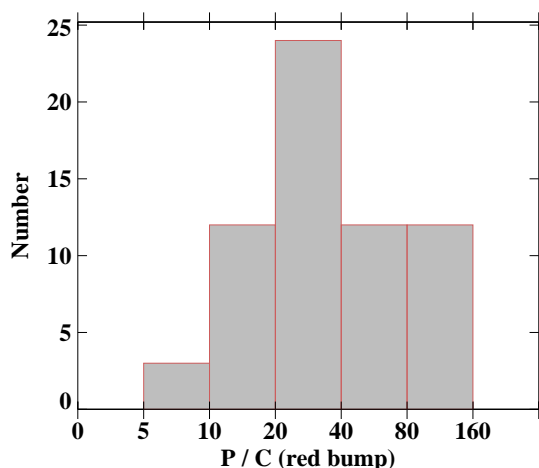


**Fig. 3:** Histogram of the parameter  $P/C$  for pixels with positive detection of the red bump. The scale of the  $x$  axis starts at a value of 5 and then every bin doubles the previous one.

more easily. For this reason, we can only observe the red bump when this contamination is not very high, and then the observed EW ( $H\alpha$ ), not corrected by the presence of other non-ionising populations, approaches the EW predicted by the models for populations younger than 6 Myr. For instance, according to POPSTAR models at solar metallicity, EW ( $H\alpha$ )  $\sim 60$  Å for a starburst with age  $\tau \sim 5.8$  Myr.

Finally, we did not find candidates with red bump emission in regions other than those where the blue bump was detected. This is expected since, at the distance where our target galaxies are located (from  $\sim 10$  Mpc to  $\sim 300$  Mpc) we can only resolve sizes larger than  $\sim 100$  pc. Actually, the red WR bump has been observed in the absence of blue bump detection in very few occasions, and always at high spatial resolution ( $\sim 10$  pc; Westmoquette et al. 2013).

## 4. Properties of the WR population in the CALIFA survey

### 4.1. The catalogue of WR-rich regions

The selection procedure presented in Sec. 3 allow us to build a mask per galaxy pinpointing the location of those pixels satisfying criteria 1–5. We report the detection of regions with positive WR emission in a total of 25 galaxies. The main properties of these WR galaxies are listed in Table 1. Our catalogue of WR galaxies represents somewhat over 4% of the initial galaxy sample, which we recall is representative of the galaxy population in the Local Universe. As the CALIFA sample was not purposely selected to contain only galaxies with strong star formation episodes, a small percentage of galaxies with regions showing strong WR signatures is expected.

The WR host galaxies found are typically spirals and nearby blue dwarf galaxies with low inclination angles. Interestingly, 13 out of the 25 WR galaxies (52%) are related to galaxy interaction processes (galaxy pairs, signs of recent past interaction, or galaxies undergoing a merger). Also the majority of the WR galaxies analysed by López-Sánchez (2010) are also experiencing some kind of interaction.

It is surprising to find WR emission in an isolated Sa galaxy (NGC 1056), with low disc star formation activity than later type galaxies (Giuricin et al. 1994; Plauchu-Frayn et al. 2012), and in a dwarf elliptical (IC 0225; also detected in B08a, WR346). In fact, this dwarf galaxy is a peculiar object showing a blue core, something which is quite rare in this kind of objects (Gu et al. 2006; Miller & Rudie 2008).

We identified a total of 44 WR-rich regions within the 25 galaxies listed in Table 1, individual WR regions per galaxy are numbered R1, R2, etc. Not all the WR regions are located in the centre of the galaxies, but rather they are distributed in the circumnuclear regions or found in external  $H\alpha$  clumps (e.g. NGC 5665). Fig. 4 shows the  $H\alpha$  map of the galaxy NGC 4470, where 3 WR regions have been identified. Similar maps for the rest of the galaxies are shown in Fig. A.1. A third of the WR regions are located at projected distances further than half an effective radius, and the majority of them lies within one

**Table 1:** Catalogue of galaxies showing WR features using the CALIFA survey data

Galaxy	$D_L$ (Mpc)	AR	DEC	Morph. type	Stage	$i = \cos^{-1} (b/a)$ (deg)	$M_B$ (mag)
(1)	(2)	(3)	(4)	(5)	(6)	(7)	(8)
IC 0225	21.3	02h 26m 28.2s	+01° 09m 39.2s	dE	I	30	-17.1
IC 0776	33.9	12h 19m 3.1s	+08° 51m 23.5s	Sdm	I	53	-18.7
NGC 0216	21.1	00h 41m 27.2s	-21° 02m 40.4s	Sd	I	70	-16.7
NGC 1056	21.6	02h 42m 48.2s	+28° 34m 30.3s	Sa	I	61	-19.6
NGC 2604	29.0	08h 33m 23.0s	+29° 32m 21.1s	Sd	M	47	-19.7
NGC 3353	12.7	10h 45m 22.1s	+55° 57m 39.4s	BCD/Irr	M	47	-18.4
NGC 3381	22.5	10h 48m 24.9s	+34° 42m 43.1s	SBd	I	47	-19.4
NGC 3773	12.7	11h 38m 12.8s	+12° 06m 44.4s	dE/dS0	I	29	-18.2
NGC 3991	44.3	11h 57m 31.6s	+32° 20m 29.4s	Sm	M	74	-20.1
NGC 3994	42.7	11h 57m 36.9s	+32° 16m 41.3s	SABbc	M	61	-20.2
NGC 4470	32.2	12h 29m 37.8s	+07° 49m 27.9s	Sc	I	47	-18.6
NGC 4630	9.4	12h 42m 31.1s	+03° 57m 37.7s	IBm	I	39	-18.0
NGC 5145	17.0	13h 25m 13.8s	+43° 16m 03.2s	S?	I	52	-19.5
NGC 5630	36.7	14h 27m 36.9s	+41° 15m 28.1s	SBdm	M	67	-19.6
NGC 5665	30.8	14h 32m 25.7s	+08° 04m 45.3s	SABc	M	46	-19.7
NGC 5953	27.6	15h 34m 32.4s	+15° 11m 38.8s	Sa	M	28	-18.8
NGC 5954	26.5	15h 34m 35.0s	+15° 12m 01.5s	SABc	M	41	-18.4
NGC 6090	123.7	16h 11m 40.6s	+52° 27m 24.9s	Sd pec	M	65	-20.9
NGC 7469	67.7	23h 03m 15.6s	+08° 52m 27.6s	SAB(s)dm	M	45	-21.2
UGC 00312	59.3	00h 31m 23.9s	+08° 28m 02.2s	SBd	M	63	-20.3
UGC 10297	32.1	16h 15m 28.9s	+18° 54m 16.6s	Sc	I	83	-19.5
UGC 10331	62.2	16h 17m 21.0s	+59° 19m 14.0s	SABc	M	75	-19.2
UGC 10650	41.1	17h 00m 14.6s	+23° 06m 24.8s	Scd	M	80	-18.8
UGC 6320	14.8	11h 18m 17.2s	+18° 50m 50.5s	S?	I	36	-17.8
UGC 9663	33.2	15h 01m 13.6s	+52° 35m 44.9s	Im	I	41	-18.2

**Notes.** Column (1): name of galaxy. Column (2): luminosity distance, taken from NED<sup>a</sup>. Columns (3) and (4): Right Ascension and declination of the centre of the galaxy. Columns (5) and (6): morphological type and stage of the galaxy (isolated, I, or merging, M). They were generally inferred by combining the independent visual classifications of several members of the CALIFA collaboration (see Walcher et al. 2014). For some galaxies references from the literature were taken (NED; IC 0225, Gu et al. 2006; IC 0776, Garcia-Lorenzo et al. 2014; NGC 3353, Sánchez-Portal et al. 2000; NGC 3373, Dellenbusch et al. 2008). Columns (7) and (8) inclination angle ( $i$ ) and B absolute magnitude, taken from NED.

<sup>a</sup> <http://ned.ipac.caltech.edu/>

effective radius (see Fig. 5, left). The WR regions sometimes cover a fraction of the total area that is normally considered a H II region (e.g., UGC 9663). In some cases, the WR regions are not apparently associated with an H $\alpha$  clump or a H II-like region, but rather located within the H $\alpha$  diffuse emission areas (e.g., R4 in NGC 5665). This suggests that some H II regions are not resolved with our IFS data. For example, the H II regions in the circumnuclear starburst in NGC 5953 (Casasola et al. 2010) are not resolved here but their WR emission has been detected. The main ionising source of these regions usually is young, massive stars, as inferred from the diagnostic BPT diagram (Baldwin et al. 1981) shown in Fig. 5 (middle panel). Only the line ratios of one WR region is very close to the location of the AGN domain. This object is the nucleus of NGC 7469, a well known Seyfert 1 galaxy with a circumnuclear starburst (Cutri et al. 1984; Heckman et al. 1986; Wilson et al. 1986), interacting with its companion IC 5283. Note that the systematics of this effect could have produced a bias in searches of WR features with SDSS or other surveys of nearby galaxies (see e.g. Kehrig et al. 2013; Shirazi & Brinchmann 2012).

The main properties of the catalogue of the selected WR regions are listed in Table 2. Given that WR stars reside in H II regions we tried, if possible, to associate the WR region with an H $\alpha$  clump in order to define their radius. As expected, the H $\alpha$  equivalent widths of these regions are close to or higher than 100 Å. It is interesting to note that the distribution of EW (H $\alpha$ ) does not peak at the highest values, but within the range 125–160 Å, and then it decreases (see Fig. 5, right). This is consistent with the fraction of star-forming galaxies that contain WR features as a function of EW (H $\beta$ ) reported in B08a, where the curve reaches a maximum value and then turns over. This turnover is expected to happen when either EW (H $\beta$ ) or EW (H $\alpha$ ) (good indicators of the age of young populations) sample burst ages that are short relative to the starting time of the WR phase (after 2–3 Myr). Obviously, our measured equivalent widths actually represent lower-limits to the real values due to the presence of underlying continuum of non-ionising populations. That is the reason why, according to POPSTAR models, our peak represents ages of  $\tau \sim 5.5$  Myr, practically when the WR phase is about to end. Yet, the real shape of the curve or the distribution of equivalent widths (i.e., in this study) should be similar to



**Table 2:** Sample of regions found with positive detection of WR features

Galaxy	Region	$\Delta\text{AR}$	$\Delta\text{DEC}$	$d / r_{\text{eff}}$	$r$	$\varepsilon$	$\varepsilon_{\text{orig}}$	$\text{EW}(\text{H}\alpha)_{\text{obs}}$	$\text{H}\alpha$	Class	Red
(1)	ID	(arcsec)	(arcsec)	(5)	(pc)	(7)	(8)	( $\text{\AA}$ )	clump	(11)	bump
	(2)	(3)	(4)		(6)			(9)	(10)		(12)
IC 0225	R1	1.7	0.0	0.0	346	10.4	6.3	121	1	1	0
IC 0776	R1	12.6	6.5	0.4	547	9.0	6.6	421	1	1	0
NGC 0216	R1	-4.7	-16.9	0.6	470	11.7	6.3	86	1	1	0
	R2	-2.0	-8.9	0.3	180	11.0	4.6	25	0	0	0
NGC 1056	R1	-1.7	-3.6	0.3	554	9.7	3.8	53	1	0	0
NGC 2604	R1	1.8	-0.3	0.0	421	13.9	9.0	139	1	1	0
NGC 3353	R1	-0.5	0.7	0.1	372	29.1	11.7	317	1	1	1
NGC 3381	R1	-0.8	-0.4	0.0	365	31.2	10.5	115	1	1	0
NGC 3773	R1	2.3	-0.4	0.0	237	24.0	11.8	148	1	1	1
NGC 3991	R1	-1.0	-6.7	0.4	956	13.0	5.9	154	1	1	1
	R2	1.8	0.8	0.1	750	17.0	8.4	229	1	1	1
NGC 3994	R1	1.0	-7.8	0.8	428	10.2	5.5	109	1	1	0
	R2	-5.4	-7.2	1.0	343	8.6	4.4	57	1	0	0
	R3	-0.1	7.9	0.8	343	7.8	4.2	66	1	0	0
NGC 4470	R1	6.4	-10.0	0.8	482	11.3	5.0	26	1	1	0
	R2	11.8	-3.8	0.8	519	9.8	5.0	58	1	1	0
	R3	1.3	10.9	0.7	432	9.5	4.2	68	1	0	0
NGC 4630	R1	-1.2	-0.2	0.0	133	14.1	6.7	168	1	1	0
NGC 5145	R1	8.2	-0.3	0.6	172	9.4	4.6	54	0	0	0
NGC 5630	R1	-10.0	3.8	0.4	849	8.8	5.4	72	1	1	0
NGC 5665	R1	5.0	-6.0	0.4	262	10.1	4.0	46	0	0	0
	R2	6.9	-1.0	0.3	468	11.7	5.2	125	1	1	0
	R3	24.4	-1.1	1.2	556	16.6	11.3	192	1	1	0
	R4	-3.5	-0.9	0.2	262	11.1	4.4	38	0	0	0
	R5	-5.9	2.5	0.3	468	8.6	4.3	48	1	0	0
	R6	8.1	4.1	0.4	504	15.6	7.1	219	1	1	0
	R7	-3.5	8.8	0.5	476	8.8	4.9	58	1	0	0
	R8	7.2	9.8	0.6	461	9.9	4.8	101	1	0	0
NGC 5953	R1	0.5	-6.2	0.4	268	9.1	3.9	74	0	0	0
NGC 5954	R1	0.7	0.9	0.1	372	9.3	3.9	74	1	0	0
	R2	4.9	2.4	0.4	398	9.9	5.4	148	1	1	0
	R3	5.4	10.5	0.9	423	10.7	6.7	279	1	1	0
NGC 6090	R1	0.2	-1.3	0.0	1915	16.2	8.9	51	1	1	0
NGC 7469	R1	1.1	-0.7	0.0	1306	10.0	8.9	67	1	1	0
UGC 00312	R1	-3.9	-23.1	1.3	958	7.8	6.4	371	1	1	0
	R2	-0.7	-7.2	0.4	932	8.5	7.7	109	1	1	0
	R3	2.3	-1.2	0.1	848	7.0	3.8	83	1	0	0
UGC 10297	R1	-1.1	16.2	0.6	432	8.7	6.9	231	1	1	0
UGC 10331	R1	2.5	-2.0	0.1	1107	8.8	5.4	161	1	1	0
	R2	-4.3	0.8	0.2	1082	10.7	6.4	137	1	1	0
UGC 10650	R1	0.3	-0.9	0.1	669	13.0	8.5	165	1	1	0
UGC 6320	R1	1.7	-0.3	0.1	295	29.1	12.4	256	1	1	1
	R2	1.1	-6.5	0.2	284	9.4	6.1	216	1	1	0
UGC 9663	R1	15.1	8.4	0.6	598	10.0	7.6	699	1	1	0

**Notes.** Column (1): name of the galaxy. Column (2): region identification number. Column (3): offset in Right Ascension from the centre of the galaxy. Column (4): offset in declination from the centre of the galaxy. Column (5): projected distance to the centre of the galaxy, normalised to the effective radius. Column (6): radius of the associated H $\alpha$  clump (if not possible association, radius of the region), derived as  $r = \sqrt{A/\pi}$ , where A corresponds to the number of pixels that form the region (note that each pixel represent an area of 1 arcsec<sup>2</sup>). Column (7):  $\varepsilon$  for the integrated spectrum of the region, after the subtracting the underlying stellar emission with STARLIGHT (see text). Column (8): same as (7), but for the observed integrated spectrum. Column (9): H $\alpha$  equivalent width of the observed integrated spectrum. Column (10): flag indicating whether a given region belongs to an H $\alpha$  clump (1) or to the more extended H $\alpha$  emission of the galaxy (0). Column (11): adopted class for the detection significance of the WR features in the regions. Column(12): flag indicating if the red bump is detected (1) or not (0).



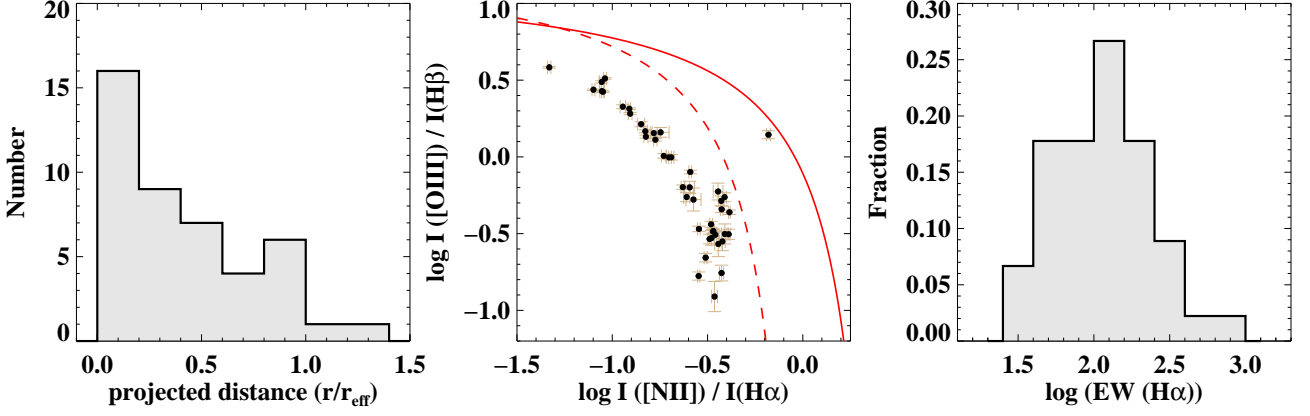


**Fig. 5: Left:** distribution of the WR region projected distance to the galaxy centre, normalized to the effective radius of the galaxy. **Middle:**  $[\text{O III}]\lambda 5007/\text{H}\beta$  vs.  $[\text{N II}]\lambda 6583/\text{H}\alpha$  diagnostic diagram (usually called the BPT diagram as described by Baldwin et al. 1981) for the selected regions. The solid and dashed lines indicate the Kewley et al. (2001) and Kauffmann et al. (2003) demarcation curves, respectively. These lines are usually used to distinguish between classical star-forming objects (below the dashed-line) and AGN powered sources (above the solid-line). Regions between both lines are considered to be of composite ionising source. **Right:** Distribution of the observed equivalent width of  $\text{H}\alpha$  in logarithmic units for the selected WR regions.

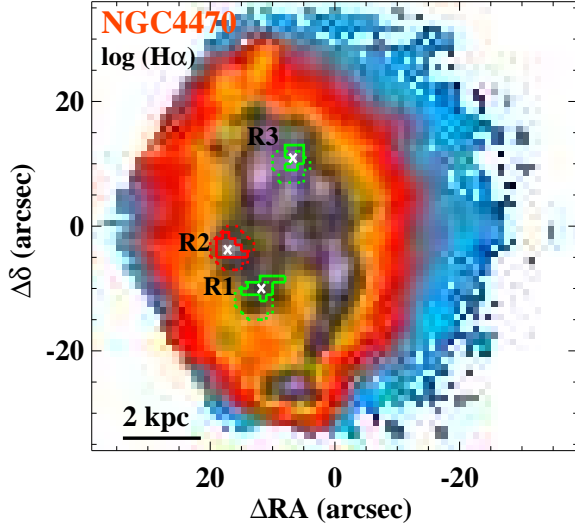


**Fig. 4:**  $\text{H}\alpha$  maps with logarithmic intensity scale of the galaxies with detected WR emission within the labelled regions enclosed by the green and red continuum contours. The pointed contours correspond to the associated  $\text{H}\alpha$  clump identified using HIIEXPLORER (Sánchez et al. 2012b), whenever the emission of the  $\text{H}\alpha$  clump is more extended than that of the WR region. A cross indicates the barycenter of the region. The scale corresponding to 2 kpc is drawn at the bottom-left corner. North points up and East to the left.

the shapes reported. As already seen in the previous section with the spectra of the pixels, we have detected the red bump in regions with higher EWs than average (150–300 Å). Taking into account that both bumps are originated in populations with similar age, this suggests that in order to better observe the red bump a lower contamination of the continuum by underlying non-ionising populations seems to be necessary.

For each WR region detected we added the spectra of all the corresponding spaxels in order to increase the S/N and perform a

detailed analysis of its properties. We derived the star formation history (SFH) of the WR region using the STARLIGHT code in order to subtract the underlying stellar continuum. At this time we used a full set of several hundreds of stellar templates to perform a better modelling of their SFH.

We divided our WR region sample in two classes depending on the significance level of the observed integrated spectra,  $\epsilon_{\text{orig}}$ . As shown in Fig. 6 the continuum is not only composed by noise but also by real absorption and emission stellar features. This fact is very notorious around 4500 Å, where the fitted continuum (solid orange line) follows well the observed continuum (solid green line) in the case of R1 in NGC 1056. Hence, the *rms* computed using this continuum is higher than the one obtained using the subtracted fitted spectrum and hence it induces an increase of the significance level. However, when  $\epsilon_{\text{orig}}$  is very low (e.g., region R1 in NGC 1056),  $\epsilon$  is also higher because the WR feature is highly enhanced. We can also see that in this situation the continuum subtraction at the level of the emission feature is not very well achieved. Although slight deviations from a zero-valued horizontal line for the subtracted continuum is expected due to fluctuations of the noise, in cases such as R1 in NGC 1056 the resulting subtracted continuum has a considerable slope. Therefore, the emission and shape of the WR feature extremely depends on the model subtraction when its detection level is close to the noise level in the observed spectrum. The higher the significance level in the observed spectrum, the lower the dependence on the model subtraction. For instance, for the spectrum of R1 in NGC 3773,  $\epsilon$  is higher than  $\epsilon_{\text{orig}}$  by a factor of 2, but this increase practically comes from the improvement of the continuum emission. The shape and area of the WR emission feature is very similar in the observed and subtracted spectrum.

Following this reasoning, we define as class-0 regions those with  $\epsilon_{\text{orig}} < 5$ , and class-1 regions as those with higher significance level on the observed spectrum. Hence, with this subdivision we can distinguish between regions whose WR emission features highly depend on the continuum subtraction and those whose dependence is either not very significant or even negligible. Under this classification scheme, 14 regions are class-

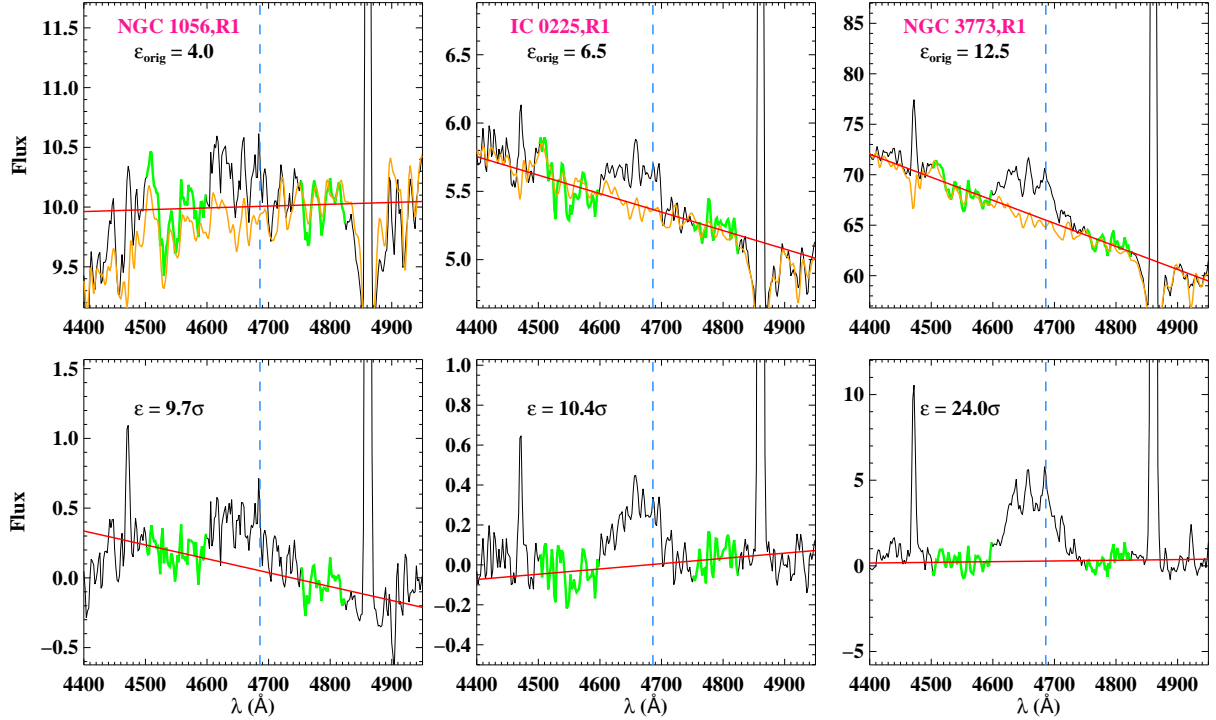


**Fig. 6:** Examples of the integrated observed spectra around the blue WR bump for three selected regions: R1 in NGC 1056 (left), R1 in IC 225 (middle) and R1 in NGC 3773 (right). The blue vertical line shows the location of the He II  $\lambda 4686$  line. The significance level ( $\epsilon_{\text{orig}}$ ) is given on the left-top corner. The red solid line shows a linear fit to the continuum. The green sections of the spectrum correspond to those spectral ranges used to compute the *rms*. The fitted continuum spectrum with STARLIGHT is overplotted in orange. **Bottom:** The corresponding continuum-subtracted spectra derived for each of the three selected regions. The value of  $\epsilon$  is provided in each case. The flux is given in units of  $10^{-16} \text{ erg s}^{-1} \text{ cm}^{-2} \text{ \AA}^{-1}$ .

0 regions and the rest (30) are class-1 regions. Table 2 also lists this subdivision.

Finally, Table 2 indicates those regions with a positive detection of the red bump. In this case, the significance level of the detection is generally higher than 20, but only five WR regions with red bump have been found in our sample.

#### 4.2. Multiple line-fitting of the WR features

The exercise explained in the previous section showed that in some cases WR emission features show up after stellar continuum subtraction in regions where there is a barely significant detection in the originally observed spectrum. In those cases, the emission line fluxes can be misleading since we are dealing with faint emission features at a continuum level where the uncertainties and systematics are not well understood. We therefore analysed WR features found *only* in class-1 regions, avoiding extremely model-dependent results (although class-0 regions still make a sample of promising candidates).

The blue bump is quite a complex emission structure formed from the blend of broad stellar lines of helium, nitrogen and carbon: He II  $\lambda 4686$ , N V  $\lambda\lambda 4605, 4620$ , N III  $\lambda\lambda 4628, 4634, 4640$ , and C III /C IV  $\lambda\lambda 4650, 4658$  (Conti & Massey 1989; Guseva et al. 2000; Crowther 2007). Furthermore, a number of nebular emission lines, such as the narrow He II  $\lambda 4686$  emission line, [Fe III]  $\lambda\lambda 4658, 4665, 4703$ , [Ar IV]  $\lambda\lambda 4711, 4740$ , He I  $\lambda 4713$  and [Ne IV]  $\lambda 4713$  are often superimposed on the broad features (Izotov & Thuan 1998; Guseva et al. 2000). This makes the disentangling of the

individual fluxes rather challenging. These nebular emission lines within the bump should be properly removed and not included in the flux of the broad stellar lines.

In the last years, multiple-Gaussian line fitting procedures have been performed in order to fit this complex feature (e.g., B08a; López-Sánchez & Esteban 2010; MC14b). Following similar prescriptions used in those studies, we performed an automatic procedure to achieve a satisfactory fit in each case:

1. The code fits a linear plus a Gaussian function to the broad He II  $\lambda 4686$ , to a broad feature centred at  $\sim 4645 \text{ \AA}$ , and to the two brightest nebular lines within this spectral range, [Fe III]  $\lambda 4658$  and the narrow He II  $\lambda 4686$ . The chosen continuum windows are the spectral ranges 4500–4550 and 4750–4820  $\text{\AA}$ . The central wavelength of the Gaussian located at 4645  $\text{\AA}$  is set free within 15  $\text{\AA}$ . In that way, the code selects which blend is better observed, either the component centred around the nitrogen lines ( $\sim 4634 \text{ \AA}$ ) or the one centred around the carbon lines ( $\sim 4650 \text{ \AA}$ ). The width ( $\sigma$ ) of the narrow (i.e., nebular) lines is fixed to that of H $\beta$  while the width of the broad components are set free with a maximum value of 22  $\text{\AA}$  (FWHM  $\sim 52 \text{ \AA}$ ), which corresponds to a FWHM of about 3300 km/s. This is appropriate taking into account the spectral resolution of the data (FWHM  $\sim 400 \text{ km/s}$ ) and the typical upper limit adopted to the width of individual WR features (Smith & Willis 1982; Crowther 2007; B08a). If the code cannot successfully fit a nebular line (due to the absence of if or low *SNR*), that component is discarded in the next step.

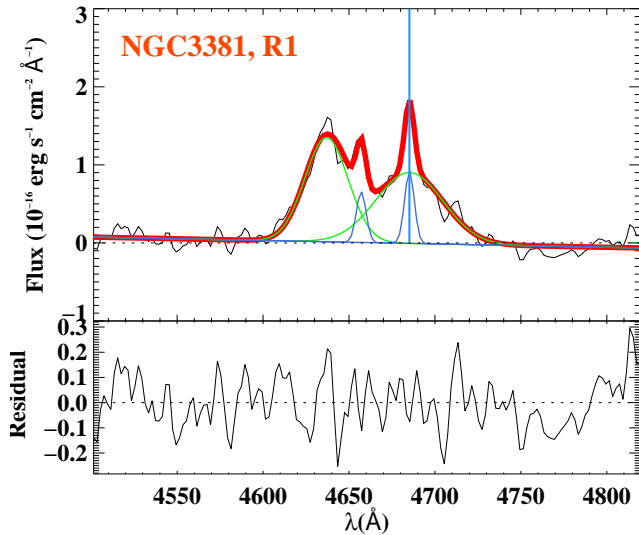


**Fig. 7:** Example of the multiple-line fit of WR features for the region found in NGC 3381. An almost horizontal blue line denotes the resulting continuum of the fit. The total fitted continuum plus emission lines on the blue bump is drawn by a thick-red line. The nebular (blue) and broad stellar (green) components of the fit are also drawn. The vertical blue line indicate the position of the He II  $\lambda 4686$  line. An auxiliary plot shows in black the residuals (in flux units) after modelling all the stellar and nebular features.

2. If the width of the broad component centred at  $4645 \text{ \AA}$  equals the maximum adopted value, a broad component around  $4612 \text{ \AA}$  is included in the fit. If the added component is not successfully fitted, it is discarded.
3. Next, the *rms* of the continuum is compared to the peak of the residuals. If this peak is higher than  $4 \times \text{rms}$  within the spectral range  $4600\text{--}4750 \text{ \AA}$ , a new component is added. If the central wavelength of the new component is shorter than  $4650 \text{ \AA}$ , it will represent a broad emission line (in a few cases two distinct components are fitted, once centred at around  $4634 \text{ \AA}$  and another at around  $4650 \text{ \AA}$ ). If the central wavelength of the new component is longer than  $4650 \text{ \AA}$ , it will be considered as a narrow line (i.e., a nebular line).
4. Finally, the previous step is done iteratively, adding each time a new component, until the peak is lower than  $4 \times \text{rms}$ .

This procedure was run 50 times for each WR region, which is the total number of times we applied the STARLIGHT fit to subtract the stellar continuum. In that way, we added to the error budget the uncertainty of the continuum subtraction. Fig. 7 shows an example of our procedure using the fit to R1 in NGC 3381. The fits obtained to the rest of WR regions are shown in Fig. A.2. In general, between three and six components are needed to properly fit the WR features. The derived uncertainties of the fits range between 10 and 50%. The intensities derived for the broad features and the nebular He II  $\lambda 4686$  emission line are compiled in Table 3. In general, the flux of the broad blue bump is of the order of 10% or lower of that of H $\beta$ .

In the case of R1 in NGC 7469, which is the nucleus of a Seyfert 1, we did not apply any continuum subtraction and just performed the fitting to the observed spectrum. Most Seyfert nuclei present a featureless ultraviolet and optical continuum following a power-law,  $f_\nu \propto \nu^{-\alpha}$ , attributed to a non-thermal

source (Osterbrock 1978). Although within a diameter  $\geq 2 \text{ kpc}$  the optical continuum is probably dominated by the stellar emission, its modelling at the level of the weak emission of the WR features is quite poor due to the presence of a power-law component, not included in the stellar libraries used in STARLIGHT. In any case, the significance level of the WR feature in the observed spectrum of this source is high enough ( $\epsilon_{\text{orig}} = 8.9$ ; see Table 2) so that a proper correction due to the continuum subtraction would not probably alter significantly the emission shape of the WR feature.

Regarding the red bump, basically two broad stellar lines form this broad emission feature, C IV  $\lambda\lambda 5801, 5812$  (van der Hucht 2001; Ercolano et al. 2004). Given the broadness of these stellar lines, the auroral [N II]  $\lambda 5755$  emission line is usually superposed on the red bump. Therefore, we fitted this narrow line together with a broad component centred at  $5808 \text{ \AA}$ , setting the central wavelength of this broad component free within  $20 \text{ \AA}$ . The fits are presented in Fig. A.3. We note that assuming a single broad component provided better results than fitting two close broad components. As we did for fitting the blue bump, an upper limit to the width of the broad component was needed. Hence, we adopted an upper limit of  $\sigma = 30 \text{ \AA}$  (FWHM  $\sim 70 \text{ \AA}$ ). Changing this value by  $5 \text{ \AA}$  induces a variation of  $\sim 10\%$  in the integrated flux. We tried to include a fit to the C III  $\lambda 5696$  emission line, which is mainly originated in carbon WR subtypes, but given the noisy residual spectrum, even in the case of NGC 3773 (see Fig. A.3), no successful fit could be achieved with an uncertainty of less than 50%. Finally, this analysis does not include a fit to the nebular He I  $\lambda 5876$  emission line since, after the continuum subtraction, some residual emission up to  $\sim 5920 \text{ \AA}$  was still found. The intensities derived for the red bump are listed in Table 3, being only a few percent of the H $\beta$  emission.

## 5. Discussion

### 5.1. Nature and number of WR stars

Learning about the nature of the WR population from the measured lines that form the blue and red bumps is not an easy task. For instance, the broad He II  $\lambda 4686$  and the blue bump emission are mainly linked to WN stars. However, some emission from WC stars may also be expected in the blue WR bump (e.g., Schaerer & Vacca 1998), so all WR types contribute to this broad emission. The broad C IV  $\lambda\lambda 5801, 5812$  emission feature essentially originates in WC stars (mainly in early-types, WCE). However, given that this feature is harder to detect than the blue bump, its non-detection does not necessarily imply the absence of WC stars. Other lines that are directly linked with other WR subtypes (e.g., O VI  $\lambda\lambda 3811, 3834$ , which are related to WO types) are not detected either. Finally, both WN and WC stars contribute to the emission of the broad N III  $\lambda\lambda 4628, 4634, 4640$  (WN) and C III / C IV  $\lambda\lambda 4650, 4658$  (WC) blends. Following MC14b, we consider these steps to identify the different sub-types of WRs that cause the WR bump emission for a given region and estimate their approximate number:

- Although He II lines are also produced by O stars with ages  $\tau \lesssim 3 \text{ Myr}$  (Schaerer & Vacca 1998; Massey et al. 2004; Brinchmann et al. 2008b), we assume that all the emission of the He II  $\lambda 4686$  line comes from WRs.



- The luminosity of WN late-type stars (WNL), the main contributors to the emission of the broad He II  $\lambda 4686$  emission, is not constant and can vary within factors of a few. Given the reported metallicity dependence of this broad emission, we use the approach proposed by López-Sánchez & Esteban (2010) to estimate the luminosity of a single WNL,  $L_{\text{WNL}}(\text{He II } \lambda 4686)$ , as a function of metallicity:

$$L_{\text{WNL}}(\text{He II } \lambda 4686) = (-5.430 + 0.812x) \times 10^{36} \text{ erg s}^{-1} \quad (2)$$

with  $x = 12 + \log(\text{O}/\text{H})$ .

- The N V  $\lambda\lambda 4605, 4620$  emission originates in early-type nitrogen stars (WNE). The mean luminosity of a single Large Magellanic Cloud WNE star is, with a dispersion of a factor of 2, about  $1.6 \times 10^{35} \text{ erg s}^{-1}$  (Crowther & Hadfield 2006). These stars also contribute to the He II  $\lambda 4686$  emission in about  $8.4 \times 10^{35} \text{ erg s}^{-1}$ .
- Given that we do not observe the C III  $\lambda 5696$  line, mainly originated in late-type WC stars, we assume that the red bump emission is mainly produced due to the presence of WCEs. We also use the approach proposed by López-Sánchez & Esteban (2010) to estimate the luminosity of this time a single WCE ( $L_{\text{WCE}}$ , C IV  $\lambda 5808$ ), as a function of metallicity:

$$L_{\text{WCE}}(\text{He II } \lambda 5808) = (-8.198 + 1.235x) \times 10^{36} \text{ erg s}^{-1} \quad (3)$$

with  $x = 12 + \log(\text{O}/\text{H})$ . These stars also contribute to the emission of the broad He II  $\lambda 4686$  line. The estimation of the contribution of a single WCE to this emission feature is explained in the following item.

- As mentioned before, the non-detection of the red bump does not guarantee that there are not WCs. MC14b estimated an upper-limit to the number of WC stars in NGC 3310 to be in the range 5–20% of the number of WN stars. There, in general  $\text{EW}(\lambda 4650) < \text{EW}(\lambda 4686)$ . However, as can be seen in Table 3, in the current study  $\text{EW}(\lambda 4650)$  is of the order of (or in some cases even higher than)  $\text{EW}(\lambda 4686)$ . This points towards a number of WC stars quite higher than just the 5%. Under these circumstances, we have made a rough estimation of the number of WCEs even if no red bump was detected. To do that, a system of two equations with two unknowns has to be solved:

$$\begin{cases} x \times L_{\text{WNL}}(\text{He II}) + y \times L_{\text{WCE}}(\text{He II}) = L(4686) \\ x \times L_{\text{WNL}}(\text{N III}) + y \times L_{\text{WCE}}(\text{C III/C IV}) = L(4650) \end{cases} \quad (4)$$

where  $L(4686)$  and  $L(4650)$  refer to the measured flux of the He II  $\lambda 4686$  and the  $\lambda 4650$  (including N III  $\lambda\lambda 4628\text{--}34\text{--}41$  and C III/C IV  $\lambda\lambda 4650\text{--}58$ ) broad features, respectively;  $L_{\text{WNL}}(\text{He II})$  and  $L_{\text{WCE}}(\text{He II})$  correspond to the luminosity of a single WNL (from Eq. 2) and a single WCE star in the  $\lambda 4686$  broad feature, respectively;  $L_{\text{WNL}}(\text{N III})$  and  $L_{\text{WCE}}(\text{C III/C IV})$  indicate the luminosity of a single WNL ( $3.8 \times 10^{35} \text{ erg s}^{-1}$ ; Crowther & Hadfield 2006) and a single WCE star in the  $\lambda 4650$  broad feature, respectively; and the unknowns  $x$  and  $y$  are the number of WNL and WCE stars.

As reported in Crowther & Hadfield (2006), the combined C III  $\lambda 4650$  + H II  $\lambda 4686$  flux of LMC WC4 stars averages around  $49 \times 10^{35} \text{ erg s}^{-1}$ . In our study, 12% of this value is assigned to a contribution to the  $\lambda 4686$  feature whereas the remaining 88% is assumed for the contribution to the  $\lambda 4650$  emission. We split it that way because several works

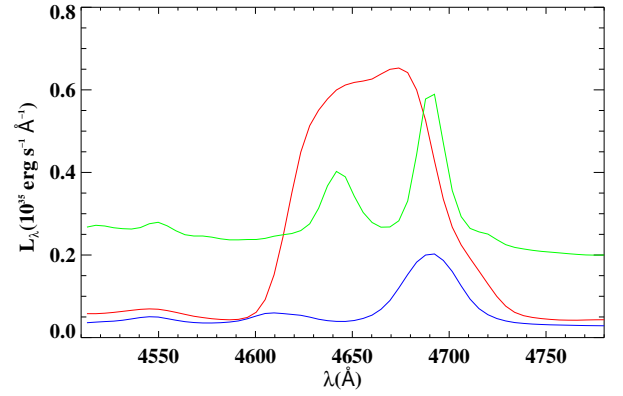


**Fig. 8:** Template of LMC WC (red), early WN (blue) and late WN (green) from Crowther & Hadfield (2006).

support that the He II  $\lambda 4686$  emission in WC stars contributes on average by 12% to the combined 4650/4686 blend (Schaerer & Vacca 1998; Smith et al. 1990), ranging from 8 to 30%. Finally, if the N V  $\lambda\lambda 4605, 4620$  emission is present in the spectra, the number of WNE stars is first obtained and then their contribution to  $L(4686)$  subtracted before solving the equation system (Eq. 4).

- Finally, we must note that the fits performed on these features are not necessarily physical, since WC lines can be much broader than the upper limits adopted, as shown in Fig. 8 (as broad as almost the entire emission bump). Depending on the contribution of WC stars to the blue bump the results might be misleading. We chose not to include another component to the fit much wider than the others and with no clue on how to constrain it (in most cases the red bump is not detected). Instead, we tried to minimize this by, instead of fitting directly this feature, assigning different contributions of this emission to the C III  $\lambda 4650$  and H II  $\lambda 4686$  fitted features, as mentioned in the previous item.

All things considered, to find the number of each type of WR, we need first to estimate the metallicity of the regions. Considering that we did not detect electron temperature sensitive lines such as the [O III]  $\lambda 4363$  for the direct determination of metallicity, we used strong line calibrations based on easily observable, optical lines. These empirical techniques have been applied to estimate oxygen abundances in objects as different as individual H II regions in spiral galaxies, dwarf irregular galaxies, nuclear starbursts and emission-line galaxies. However, caution must be taken when using the strong-line methods to derive the oxygen abundance, as some of them differ by up to 0.6 dex (see López-Sánchez et al. 2012, for a recent review). Given that some of the galaxies in our sample of WR regions are relatively close ( $D_L < 30 \text{ Mpc}$ ; see Table 1), the [O II]  $\lambda\lambda 3727, 3729$  lines do not lie in our observed spectrum. Therefore, we used a calibration based on the  $O3N2$  parameter, first introduced by Alloin et al. (1979):

$$O3N2 = \log \left( \frac{H\alpha}{[\text{N II}]\lambda 6584} \times \frac{[\text{O III}]\lambda 5007}{H\beta} \right). \quad (5)$$

We consider the calibration proposed by Marino et al. (2013), which is valid for  $12 + \log(\text{O}/\text{H}) > 8.1$  and has a dispersion somewhat lower than 0.2 dex. In any case, we compared the derived oxygen abundances with those obtained using the “counterpart” C-method, introduced by Pilyugin et al.

**Table 3:** Fluxes derived from our fitting of the WR bumps, and derived WR numbers for the class-1 WR regions identified in this study

Galaxy (1)	Region ID (2)	H $\beta$ (WR) ( $\times 10^{-14}$ cgs) (3)	c (H $\beta$ ) (4)	N v $\lambda 4612$	N/C $\lambda 4650$	Narrow He II $\lambda 4686$ I / I(H $\beta$ ) (WR) (5–9)	Blue bump	Red bump	12 + log(O/H) (O3N2) (10)	N <sub>WNE</sub> (11)	N <sub>WNL</sub> (12)	N <sub>WCE</sub> (RB) (13)	N <sub>WCE</sub> (4650) (14)
IC 0225	R1	1.62 $\pm$ 0.03	0.09 $\pm$ 0.01	–	9.3 $\pm$ 4.7	–	9.9 $\pm$ 4.6	–	8.40 $\pm$ 0.04	–	61 $\pm$ 29	–	15 $\pm$ 9
IC 0776	R1	0.67 $\pm$ 0.00	0.00 $\pm$ 0.01	–	4.1 $\pm$ 3.1	0.44 $\pm$ 0.20	3.9 $\pm$ 0.8	–	8.21 $\pm$ 0.02	–	28 $\pm$ 6	–	7 $\pm$ 5
NGC 0216	R1	3.94 $\pm$ 0.09	0.12 $\pm$ 0.01	–	10.7 $\pm$ 2.4	0.60 :	11.7 $\pm$ 1.3	–	8.33 $\pm$ 0.06	–	181 $\pm$ 18	–	40 $\pm$ 11
NGC 2604	R1	4.92 $\pm$ 0.08	0.25 $\pm$ 0.01	–	7.1 $\pm$ 1.1	0.67 $\pm$ 0.32	11.0 $\pm$ 1.3	–	8.46 $\pm$ 0.04	–	393 $\pm$ 43	–	53 $\pm$ 13
NGC 3353	R1	81.51 $\pm$ 0.54	0.19 $\pm$ 0.01	0.45 $\pm$ 0.09	2.3 $\pm$ 0.3	0.31 $\pm$ 0.06	4.5 $\pm$ 0.3	0.71 $\pm$ 0.10	8.22 $\pm$ 0.02	481 $\pm$ 92	268 $\pm$ 122	62 $\pm$ 8	68 $\pm$ 12
NGC 3381	R1	6.61 $\pm$ 0.12	0.15 $\pm$ 0.01	–	9.8 $\pm$ 0.6	1.54 $\pm$ 0.17	10.5 $\pm$ 0.7	–	8.58 $\pm$ 0.07	–	269 $\pm$ 16	–	75 $\pm$ 4
NGC 3773	R1	22.07 $\pm$ 0.31	0.07 $\pm$ 0.01	–	9.7 $\pm$ 1.7	0.71 $\pm$ 0.15	8.2 $\pm$ 0.9	6.82 $\pm$ 1.07	8.35 $\pm$ 0.04	–	216 $\pm$ 62	151 $\pm$ 22	83 $\pm$ 17
NGC 3991	R1	4.73 $\pm$ 0.07	0.02 $\pm$ 0.01	–	5.7 $\pm$ 0.5	1.32 $\pm$ 0.19	3.3 $\pm$ 0.7	4.36 $\pm$ 1.00	8.27 $\pm$ 0.04	–	187 $\pm$ 80	261 $\pm$ 56	137 $\pm$ 14
	R2	15.10 $\pm$ 0.16	0.07 $\pm$ 0.01	–	4.5 $\pm$ 0.3	0.70 $\pm$ 0.14	2.4 $\pm$ 0.3	4.13 $\pm$ 0.80	8.24 $\pm$ 0.03	–	348 $\pm$ 128	808 $\pm$ 149	353 $\pm$ 24
NGC 3994	R1	8.20 $\pm$ 0.18	0.50 $\pm$ 0.01	–	10.7 $\pm$ 1.3	–	5.9 $\pm$ 0.8	–	8.53 $\pm$ 0.05	–	592 $\pm$ 89	–	428 $\pm$ 47
NGC 4470	R1	0.44 $\pm$ 0.03	0.09 $\pm$ 0.03	–	32.5 $\pm$ 4.5	–	23.8 $\pm$ 3.7	–	8.50 $\pm$ 0.17	–	81 $\pm$ 9	–	37 $\pm$ 3
	R2	0.86 $\pm$ 0.03	0.19 $\pm$ 0.02	–	17.8 $\pm$ 2.7	–	14.2 $\pm$ 3.6	–	8.46 $\pm$ 0.09	–	97 $\pm$ 26	–	39 $\pm$ 6
NGC 4630	R1	11.01 $\pm$ 0.14	0.28 $\pm$ 0.01	–	5.0 $\pm$ 0.6	0.65 $\pm$ 0.16	6.5 $\pm$ 0.8	–	8.60 $\pm$ 0.06	–	49 $\pm$ 5	–	10 $\pm$ 1
NGC 5630	R1	1.74 $\pm$ 0.05	0.28 $\pm$ 0.02	–	8.8 $\pm$ 1.5	–	9.5 $\pm$ 1.7	–	8.37 $\pm$ 0.06	–	194 $\pm$ 34	–	44 $\pm$ 9
NGC 5665	R2	7.44 $\pm$ 0.13	0.30 $\pm$ 0.01	–	5.7 $\pm$ 0.6	–	4.9 $\pm$ 0.5	–	8.56 $\pm$ 0.05	–	260 $\pm$ 25	–	97 $\pm$ 11
	R3	1.97 $\pm$ 0.02	0.23 $\pm$ 0.01	–	8.6 $\pm$ 0.9	1.13 $\pm$ 0.21	7.2 $\pm$ 0.9	–	8.53 $\pm$ 0.03	–	100 $\pm$ 13	–	39 $\pm$ 4
	R6	12.98 $\pm$ 0.14	0.36 $\pm$ 0.01	–	5.8 $\pm$ 0.5	0.40 $\pm$ 0.15	2.9 $\pm$ 0.4	–	8.56 $\pm$ 0.03	–	226 $\pm$ 42	–	192 $\pm$ 18
NGC 5954	R2	5.28 $\pm$ 0.08	0.42 $\pm$ 0.01	–	8.6 $\pm$ 1.0	0.57 $\pm$ 0.27	5.1 $\pm$ 1.0	–	8.55 $\pm$ 0.04	–	129 $\pm$ 31	–	83 $\pm$ 10
	R3	7.67 $\pm$ 0.06	0.37 $\pm$ 0.01	–	5.5 $\pm$ 0.6	–	3.8 $\pm$ 0.4	–	8.55 $\pm$ 0.02	–	147 $\pm$ 19	–	76 $\pm$ 9
NGC 6090	R1	51.64 $\pm$ 0.76	0.55 $\pm$ 0.01	–	3.1 $\pm$ 0.3	0.72 $\pm$ 0.14	4.9 $\pm$ 0.5	–	8.55 $\pm$ 0.03	–	31023 $\pm$ 2851	–	4538 $\pm$ 623
NGC 7469	R1	98.29 $\pm$ 3.48	0.35 $\pm$ 0.02	–	12.2 $\pm$ 1.7	–	7.5 $\pm$ 2.1	–	8.48 $\pm$ 0.07	–	21772 $\pm$ 7053	–	12893 $\pm$ 1660
UGC 00312	R1	1.33 $\pm$ 0.01	0.11 $\pm$ 0.01	–	5.8 $\pm$ 2.1	0.75 $\pm$ 0.22	2.2 $\pm$ 0.9	–	8.23 $\pm$ 0.02	–	72 $\pm$ 41	–	75 $\pm$ 29
	R2	1.55 $\pm$ 0.03	0.17 $\pm$ 0.01	–	8.1 $\pm$ 1.2	–	3.4 $\pm$ 0.4	–	8.39 $\pm$ 0.04	–	122 $\pm$ 18	–	120 $\pm$ 16
UGC 10297	R1	1.21 $\pm$ 0.01	0.32 $\pm$ 0.01	–	8.0 $\pm$ 1.2	1.57 $\pm$ 0.45	10.6 $\pm$ 1.7	–	8.22 $\pm$ 0.03	–	130 $\pm$ 21	–	18 $\pm$ 4
UGC 10331	R1	4.08 $\pm$ 0.05	0.45 $\pm$ 0.01	–	6.2 $\pm$ 0.7	0.56 $\pm$ 0.26	3.8 $\pm$ 0.7	–	8.47 $\pm$ 0.03	–	438 $\pm$ 98	–	256 $\pm$ 30
	R2	2.92 $\pm$ 0.04	0.32 $\pm$ 0.01	–	7.7 $\pm$ 0.7	0.63 $\pm$ 0.23	5.3 $\pm$ 0.8	–	8.36 $\pm$ 0.03	–	476 $\pm$ 77	–	220 $\pm$ 21
UGC 10650	R1	3.29 $\pm$ 0.04	0.15 $\pm$ 0.01	–	5.9 $\pm$ 1.0	–	6.5 $\pm$ 0.7	–	8.35 $\pm$ 0.03	–	319 $\pm$ 34	–	70 $\pm$ 16
UGC 6320	R1	13.90 $\pm$ 0.12	0.13 $\pm$ 0.01	0.66 $\pm$ 0.15	4.4 $\pm$ 0.4	0.29 $\pm$ 0.11	6.6 $\pm$ 0.4	1.05 $\pm$ 0.15	8.29 $\pm$ 0.02	162 $\pm$ 35	86 $\pm$ 42	20 $\pm$ 3	33 $\pm$ 4
	R2	2.82 $\pm$ 0.03	0.13 $\pm$ 0.01	–	3.2 $\pm$ 0.8	0.55 $\pm$ 0.19	6.8 $\pm$ 0.8	–	8.29 $\pm$ 0.02	–	41 $\pm$ 4	–	2 $\pm$ 1
UGC 9663	R1	0.98 $\pm$ 0.01	0.10 $\pm$ 0.01	–	4.9 $\pm$ 1.2	0.95 $\pm$ 0.30	7.9 $\pm$ 1.4	–	8.14 $\pm$ 0.02	–	90 $\pm$ 17	–	7 $\pm$ 3

**Notes.** Column (1): name of the galaxy. Column (2): region identification number. Column (3): the extinction corrected H $\beta$  line intensity of the region showing WR features. Column (4): extinction coefficient. Columns (5–9): line intensity ratios of the broad band components of the blue bump plus the nebular He II  $\lambda 4686$  emission line and the broad component of the red bump with respect to H $\beta$ , normalized to H $\beta$  = 100. We used the law by Cardelli et al. (1989), assuming  $R_V = 3.1$  and case B recombination (Osterbrock 1989), in order to correct the emission-line fluxes for internal extinction. Column (10): gaseous oxygen abundance of the region showing WR features, obtained using the O3N2-parameter (see text). Column (11): derived number of early-type WN stars. Column (12): derived number of late-type WN stars. Column (13): derived number of early-type WC stars using the flux measurement of the red bump. Column (14): estimated number of early-type WC stars using the flux measurement of the broad  $\lambda 4650$  feature.

(2012), which is valid for all the metallicity range, obtaining consistent values within 0.1 dex. The metallicities derived using the  $O3N2$  calibration are listed in Table 3. The oxygen abundances range between  $12 + \log(O/H) = 8.2$  and  $8.6$ , with the typical value being about half of the solar value.

With this information we derived the number of WR stars for each sub-type, when possible. The number of WNE, WNL and WCE stars are compiled in the last columns of Table 3. We estimated the number of WNL and WCE stars by solving Eq. 4 in all cases, of WNE stars in just 2 cases (those showing a clear detection of the  $N\,v\,\lambda\lambda 4605, 4620$  blend) and the number of WCE stars using Eq. 3 in the five regions where the red WR bump is present in our spectra. In those cases where the red bump is detected we considered the number of WCE stars derived via the flux measurement of such bump to compute their contribution to the broad  $He\,II\,\lambda 4686$  emission. It is also convenient to mention that if we did not consider to solve the system and estimated instead the number of WNL stars by using directly Eq. 2, the resulting values would be higher by 10–20%.

The derived values span a wide range, from a few dozens in regions within the closest galaxies (NGC 4630 and UGC 6320) to more than 30 thousands in regions belonging to the most distant objects (NGC 6090 and NGC 7469). It is worth noting the detection of more than 30 thousand WRs in the nuclear region of a Seyfert 1 galaxy. It is not the first time that the coexistence of the AGN and a circumnuclear compact starburst located several hundreds of pc away has been reported (e.g., in Mrk 477 Heckman et al. 1997). In fact, the estimated number of WRs in that compact source amounts to about 30 thousands.

We can compare the estimation of the number of WCE stars in those cases where the red bump is detected,  $N_{WCE}$  (RB) and  $N_{WCE}$  (4650) in Table 3. Only in one case (NGC 3353) can we consider both values compatible within the uncertainties. A difference within a factor of two is encountered between both estimates in the remaining WR regions. This is not surprising given the uncertainties involved in these estimates, like the possible systematics when using average luminosities that range enormously in each methodology (for instance, in Crowther & Hadfield 2006 luminosities of single WC4s in LMCs range from less than 2 to more than  $4 \times 10^{36} \text{ erg s}^{-1}$ ). Finally, we remark that the number of WCEs that we obtain by solving the equation system (Eq. 4) represents generally between 15 and 25% the number of WNLs<sup>4</sup> as we expected, given that  $EW(\lambda\,4650) \geq EW(\lambda\,4686)$ . We even find some unexpected cases (e.g., R1 in NGC 3994, R6 in NGC 5665, R1 and R2 in UGC 00312) where  $EW(\lambda\,4650) > 2 \times EW(\lambda\,4686)$ , and where the percentage is higher than 40%. Again, the systematics may play an important role in these estimates. All in all, we conclude that the estimates in the number of WCEs are probably correct within a factor of two.

## 5.2. Dilution of the WR features

One of the main biases when interpreting observational data is the limitation imposed by the spatial resolution. As mentioned before, WRs are usually very localized, sometimes the emission of the associated  $H\,II$  region is significantly more extended, i.e., the spatial extent of WRs can be considerably smaller than that of the rest of the ionising population (Kehrig et al. 2013). This is one of the main reasons why the emission of WRs easily dilutes in non-resolved studies. In this section, we discuss the

effects of this dilution on the detectability and determination of the fluxes of the broad emission features when using the techniques described in this paper. Indeed, this directly affects the determination of the number of WR stars and constitutes a crucial step when interpreting the observed flux and when comparing them with stellar population models.

In several cases the spatial extent of the  $H\alpha$  clumps (i.e.,  $H\,II$  regions or aggregates) associated to our WR regions is larger than the area showing WR emission (see Fig. A.1). If we integrated the spectrum of these clumps we would expect the WR bump to either disappear or dilute significantly. Then, if we performed the multiple-fit of the WR emission features we would expect to obtain lower equivalent widths or detection significance. Several factors affect the final measured fluxes when the dilution effect is present:

- Once the bump is diluted, its detection significance level decreases; and, if it is too much diluted it can actually disappear in the observed spectrum. As mentioned in Sec. 4.2, when  $\epsilon_{\text{orig}} < 5$ , the shape of the WR feature is not very well constrained, since it is extremely model dependent on the continuum subtraction, which leads to unrealistic features. This happens, for instance, in R1 in IC 0225. When we integrate only the pixels showing WR features,  $\epsilon_{\text{orig}} = 6.3$ , and when we integrate the whole  $H\alpha$  clump  $\epsilon_{\text{orig}} = 4.2$ . In NGC 1056, the bump actually disappears in the observed spectrum ( $\epsilon_{\text{orig}} = 2.6$ ).
- If the bump dilutes, barely resolved lines (i.e., weak nebular lines, weak broad components) dissolve, thus fewer and broader components are fitted. In order to properly interpret the measurement of the fluxes of the broad bump features, we have to correct for the nebular emission lines; and, specifically for the case of the broad  $He\,II\,\lambda 4686$  line, try to isolate it from the blend at  $4640\text{--}4650\,\text{\AA}$ . This effect is illustrated in Fig. 9, for R1 in IC 0776.
- In some cases, even if the same number of components are fitted, they become broader. If the lines are broader and the peak is similar then more flux is measured.

These effects justify why we did not consider in our analysis the 0-class regions. Even if none of these effects is observed the recovered fluxes for the 0-class WR regions can vary for large factors, leading to very uncertain WR properties. Note that this does not affect the WR regions with the highest detection significance since their aperture is similar to that of the associated  $H\alpha$  clump (e.g., in NGC 3353, NGC 3773, NGC 3991). It is worth noting that dilution effects should be taken into account when deriving properties of WR populations, specially in observations with poor spatial resolution and if the sampled area is larger than the area showing WR emission.

## 5.3. Comparison with stellar population models

### 5.3.1. Definition of the sub-sample

The  $H\alpha$  emission in  $H\,II$  regions is typically more extended than the localized WR stellar emission in a given cluster, giving rise to the dilution effect discussed above, a fact that has to be taken into account when comparing spectroscopic observables with stellar population models. For instance, to make a proper comparison of the flux ratio of the blue bump to  $H\beta$ , we have to obtain the flux of  $H\beta$  from the whole  $H\,II$  spectrum, as done for instance in B08a and discussed in Kehrig et al. (2013) for Mrk 178.

Aperture effects can also deceive the comparison with models the other way round. Non-resolved  $H\alpha$  clumps with

<sup>4</sup> Should we assume the  $He\,II\,\lambda 4686$  broad emission comes entirely from WNLs.



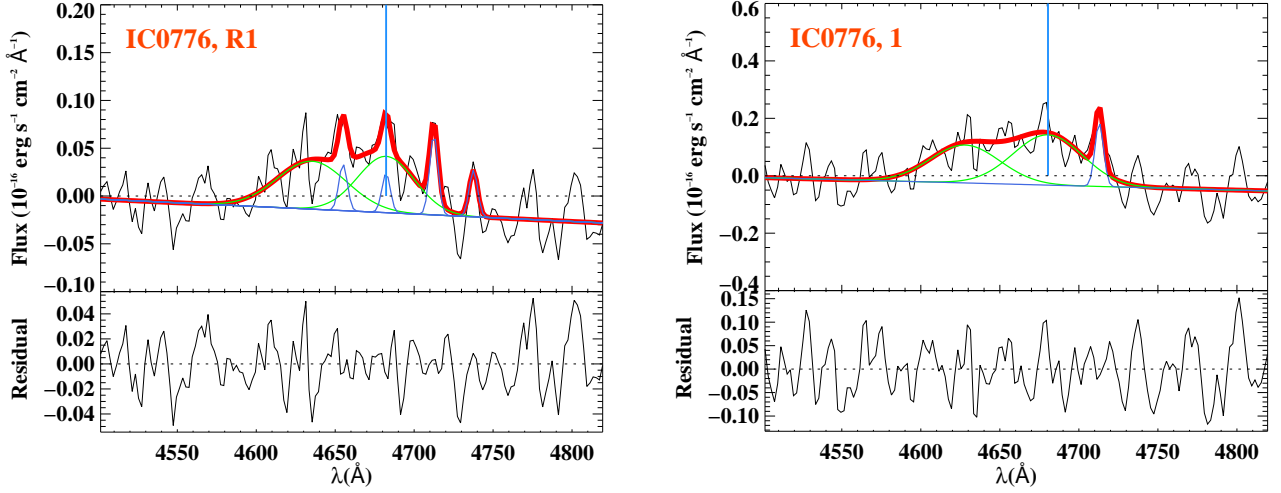


**Fig. 9:** R1 in IC 0776 as typical example showing the effects of the dilution, for the spectrum of the WR region (left) and for the spectrum of the associated H $\alpha$  clump (right). Lines and colours are the same as in fig. 7. Some structure is lost and fewer nebular lines are fitted when the WR feature is diluted. It is also noticeable that the broad lines widen.

**Table 4:** Derived properties of the WR population and WR number ratios

Galaxy	Region ID	H $\beta$ (clump) ( $\times 10^{-14}$ cgs)	c (H $\beta$ )	Blue WR bump EW (Å)	Red WR bump EW (Å)	EW (H $\beta$ ) (Å)	$\tau$ (Myr)	$\eta_0$	$N_0$	$N_{WR} / N_0$	$Q_0^{\text{Total}}$ log (cgs)	$Q_0^{\text{WR}}$ log (cgs)
(1)	(2)	(3)	(4)	(5)	(6)	(7)	(8)	(9)	(10)	(11)	(12)	(13)
IC 0225	R1	$3.23 \pm 0.07$	0.06	$1.4 \pm 0.8$	—	$31^{+3}_{-1}$	$5.5 \pm 0.3$	$0.30 \pm 0.05$	$551^{+276}_{-251}$	$0.14^{+0.22}_{-0.08}$	51.56	$51.31 \pm 0.16$
NGC 3353	R1	$81.51 \pm 0.54$	0.19	$3.8 \pm 0.4$	$0.9 \pm 0.2$	$90^{+5}_{-3}$	$4.5 \pm 0.3$	$0.25^{+0.10}_{-0.05}$	$4919^{+2430}_{-2095}$	$0.17^{+0.21}_{-0.09}$	52.52	$52.32 \pm 0.11$
NGC 3381	R1	$6.61 \pm 0.12$	0.15	$4.5 \pm 0.8$	—	$45^{+5}_{-6}$	$4.3 \pm 0.2$	$0.35^{+0.15}_{-0.10}$	$< 172$	$> 1.75$	51.92	$> 51.89$
NGC 3773	R1	$22.07 \pm 0.31$	0.07	$3.5 \pm 1.1$	$4.5 \pm 1.6$	$46^{+18}_{-3}$	$5.2 \pm 0.2$	$0.25 \pm 0.05$	$< 1139$	$> 0.19$	51.95	$> 51.91$
NGC 4630	R1	$11.01 \pm 0.14$	0.28	$3.0 \pm 0.7$	—	$49^{+7}_{-3}$	$4.3 \pm 0.5$	$0.35^{+0.15}_{-0.13}$	$252^{+138}_{-80}$	$0.24^{+0.13}_{-0.09}$	51.38	$51.19 \pm 0.04$
NGC 5954	R2	$12.03 \pm 0.20$	0.42	$0.9 \pm 0.2$	—	$41^{+4}_{-3}$	$5.5 \pm 0.3$	$0.30 \pm 0.05$	$5123^{+1018}_{-783}$	$0.04^{+0.01}_{-0.01}$	52.32	$51.77 \pm 0.06$
UGC 6320	R1	$13.90 \pm 0.12$	0.13	$4.5 \pm 0.6$	$1.1 \pm 0.2$	$74^{+9}_{-3}$	$4.8 \pm 0.2$	$0.22 \pm 0.05$	$744^{+759}_{-506}$	$0.31^{+0.85}_{-0.20}$	51.88	$51.78 \pm 0.08$
	R2	$6.64 \pm 0.07$	0.09	$1.9 \pm 0.5$	—	$79^{+23}_{-8}$	$4.8 \pm 0.2$	$0.22^{+0.13}_{-0.05}$	$1124^{+249}_{-285}$	$0.04^{+0.01}_{-0.01}$	51.56	$51.04 \pm 0.05$

**Notes.** Column (1): name of the galaxy. Column (2): region identification number. Column (3): the extinction corrected H $\beta$  line intensity of the corresponding H $\alpha$  clump. Column (4): extinction coefficient. Column (5): equivalent width of the He II  $\lambda 4686$  line measured in the WR region, corrected by the continuum emission of non-ionising populations. Column (6): same as (5) but for the broad C IV  $\lambda 5808$  line. Column (7): equivalent width of H $\beta$  measured in the H $\alpha$  clump and corrected by the continuum emission of non-ionising populations. Column (8): derived age of the ionising population using the EWs reported in (7) and the POPSTAR models. Column (9): adopted  $\eta_0$  parameter. Column (10): derived number O stars. Column (11): number ratio of WR stars with respect to the total numbers of O stars. Column (12): total Lyman Continuum flux, as derived with the H $\alpha$  luminosity (the random uncertainty is in all cases it is below 2%). Column (13): estimated Lyman Continuum flux emerging from WR stars.

sizes of several hundreds of pc or larger can harbour several H II regions. For instance, within an aperture of 1 kpc several regions in NGC 4630 are observed, but only the central region shows significant WR emission features. This can happen even at smaller apertures, such as in the giant H II region Tol 89 in NGC 5398 (Sidoli et al. 2006). Within an aperture of about 300 pc there are at least 2 complexes (A and B) of massive ( $M > 10^5 M_\odot$ ) clusters with ages within the range  $\tau \sim 2 - 5$  Myr, the most massive and youngest (B) not showing signs of WR emission. Thus, if we compare the integrated WR and H $\beta$  emission in this case, the interpretation of the properties of the population might be wrong. This gives us an idea that 100–200 pc can represent an appropriate aperture to perform this kind of studies.

In this study, we have performed this comparison for regions with a radius smaller than 400 pc (see Table 2), in order to have at least several regions at our disposal. Thus, in a few

cases (NGC 3353, NGC 3381, NGC 5954) our results may still be somehow misleading provided that there is a cluster young enough so that WRs are still not present.

### 5.3.2. WR ratios and predictions from stellar population models

Empirical results such as the ratio of WR to O stars provide sensitive tests of evolutionary models which involve complex processes (i.e., rotation, binarity, feedback, IMF, etc.) that remain not sufficiently constrained. This ratio can be roughly derived by first estimating the number of O stars using the H $\beta$  luminosity. We remind the reader that the Balmer emission in H II regions is typically more extended than the localized WR stellar emission. Therefore, in order to properly compute the number of O stars we have to use the H $\beta$  luminosity of the

whole H $\alpha$  clump where the WR emission is detected. Then, assuming a contribution to the H $\beta$  luminosity by an O7V star of  $L_{O7V} = 4.76 \times 10^{36} \text{ erg s}^{-1}$ , a first estimation of the number of such stars is obtained by  $N_{O7V} = L(H\beta)/L_{O7V}$ . Finally, the contribution of the WRs and other O subtypes to the ionising flux is corrected as explained below:

- Following Crowther & Hadfield (2006), the average numbers of ionising photons of a WN and a WC star are assumed to be  $\log Q_0^{WN} = 49.4$  and  $Q_0^{WC} = 49.5$ , respectively.
- The total number of O stars ( $N_O$ ) can be derived from the number of O7V ( $N_{O7V}$ ) stars by correcting for other O stars subtypes, using the parameter  $\eta_0$  introduced by Vacca & Conti (1992) and Vacca (1994). This parameter depends on the initial mass function for massive stars and is a function of time because of their secular evolution (Schaerer & Vacca 1998). We made a rough estimation of the age of the population using the EW (H $\beta$ ) measured on the H II region spectra. This value was corrected by the emission of non-stellar ionising population, since the STARLIGHT code provides us with the star formation history of the region (see Miralles-Caballero et al. 2014a). With the approximate knowledge of the age of the population we estimated  $\eta_0$  using the SV98 models. The strongly non-linear temporal evolution of this parameter during some time intervals (see Fig. 21 in Schaerer & Vacca 1998) causes some asymmetries in the determination of its uncertainty. Table 4 lists the derived age, corrected EW (H $\beta$ ) and estimated  $\eta_0$  for our sub-sample of regions.

With this we determined the number of O stars as:

$$N_O = \frac{Q_0^{\text{Total}} - N_{WN}Q_0^{WN} - N_{WC}Q_0^{WC}}{\eta_0 Q_0^{O7V}}, \quad (6)$$

where  $Q_0^{\text{Total}} = N_{O7V}Q_0^{O7V}$  and  $Q_0^{O7V}$  are the total and O7V number of ionising photons, respectively. We have adopted an average Lyman continuum flux per O7V star of  $\log Q_0^{O7V} = 49.0$  (Vacca & Conti 1992; Schaerer & Vacca 1998; Schaerer et al. 1999). The number of O stars and the WR to O ratio are reported in Table 4. The errors are generally large, making evident the high uncertainties involved when trying to derive these properties. In two cases (R1 in NGC 3353 and NGC 3381), the computed number of O stars is negative, a non-physical result. Nevertheless, given the large uncertainties involved in the determination of  $\eta_0$  and the number of each sub-type of WR, we have been able to provide an upper-limit within a confidence level of 90%. This allowed us to obtain a lower limit to the WR to O ratio. We remark that given the large uncertainties involved a Montecarlo simulation was run in order to obtain all the uncertainties. The median values in each simulation of  $N_O$  and  $N_{WR}/N_O$  were the same to those obtained applying Eq. 6 directly to the derived average values of its elements, except for R1 in UGC 6320. Taking advantage of the Montecarlo simulation, we realized that in this case a non-negligible percentage of estimates for  $N_O$  were negative, which indicates that we were close to the noise level to obtain a physical result. Using the Bayesian approach we restricted the distribution considering only positive  $N_O$  and then renormalized this new distribution with only physical values. We thereby obtained a more representative value for  $N_O$  by taking the median of the renormalized distribution, and which is reported in the table. The same accounts for  $N_{WR}/N_O$  for R1 in UGC 6320.

Table 4 also provides the total estimated Lyman Continuum flux and that emerging from WR stars. It is interesting to note that the contribution from the WR population is generally higher than the flux emerging from the other populations altogether. Even in those cases where the number of WR stars is almost negligible compared to that of O stars (around 4%, in NGC 5954 and in R2 in UGC 6320), the ionising flux emerging from WR populations accounts for 30% of the total Lyman Continuum budget.

We have compared our observational data with the predictions of two different theoretical model sets: (i) POPSTAR (Mollá et al. 2009; Martín-Manjón et al. 2010), a self-consistent set of models including the chemical and the spectro-photometric evolution, for spiral and irregular galaxies, where star formation and dust effects are important; and (ii) BPASS (Eldridge et al. 2008; Eldridge & Stanway 2009), which includes the binary evolution in modelling the stellar populations, that can extend the WR phase up to longer than 10 Myr. Both models use the photoionization code CLOUDY (Ferland et al. 1998) to predict the nebular emission.

The disagreement between models and data at moderate and low metallicities have been known for some time (e.g., Guseva et al. 2000; Crowther & Hadfield 2006; Pérez-Montero et al. 2010; López-Sánchez & Esteban 2010), especially when trying to explain the derived large WR to O ratios from observations. As discussed in Crowther (2007), the production of more WRs than currently favoured by the models can be achieved by including binarity in the evolutionary codes or when rotation is included in the stellar tracks. They have become promising sources for an increased WR population. In fact, several studies of samples of Galactic massive O stars support that binary interaction dominates the evolution of massive stars (e.g. Kobulnicky & Fryer 2007; Sana et al. 2012; Kiminki & Kobulnicky 2012). Eldridge et al. (2008) developed a synthesis population code, BPASS<sup>5</sup>, where binarity is included. They found out that a third of the population evolves as single stars, while the remaining two thirds correspond to interacting binaries. The inclusion of binaries led to a prolonged WR phase (up to  $\tau \sim 15$  Myr), consistent with earlier predictions by Van Bever & Vanbeveren (2003).

As observed in Fig. 10 (top) simple stellar population models (POPSTAR) are not able to reproduce for the low-metallicity regions ( $Z \sim Z_{\odot}/3$ ) either the flux ratio I (broad He II  $\lambda 4686$ ) / I(H $\beta$ ) or the EW of the blue bump corrected by the continuum emission of the non-ionising population. For the sake of completeness, we also show how the modelled tracks would move if half of the ionising photons escape from the H II regions (i.e.,  $F_L \equiv 2.0$ ) or if they are absorbed by dust grains within the nebula (i.e.,  $F_d \equiv 2.0$ ). Thus, if we allow for some Lyman photon leakage or some absorption by dust grains within the nebula, the POPSTAR models could reproduce the flux ratio. However, in any case, for three regions only the binary models could explain the relatively high blue bump equivalent widths (Fig. 10, top-right).

Reproducing the WR to O ratio, namely  $N_{WR}/N_O$ , is hard for the stellar population models, especially for the low-metallicity regions (Fig. 10, bottom-left). Besides, as mentioned in MC14b, this ratio can vary dramatically if we allow for some Lyman photon leakage, some absorption by dust grains within the nebula, or even a different IMF. Note that this variation is not the same for all regions (like in the top panel), since if EW (H $\beta$ ) increases, the age decreases and  $\eta_0$  (which is practically constant

<sup>5</sup> <http://www.bpass.org.uk/>

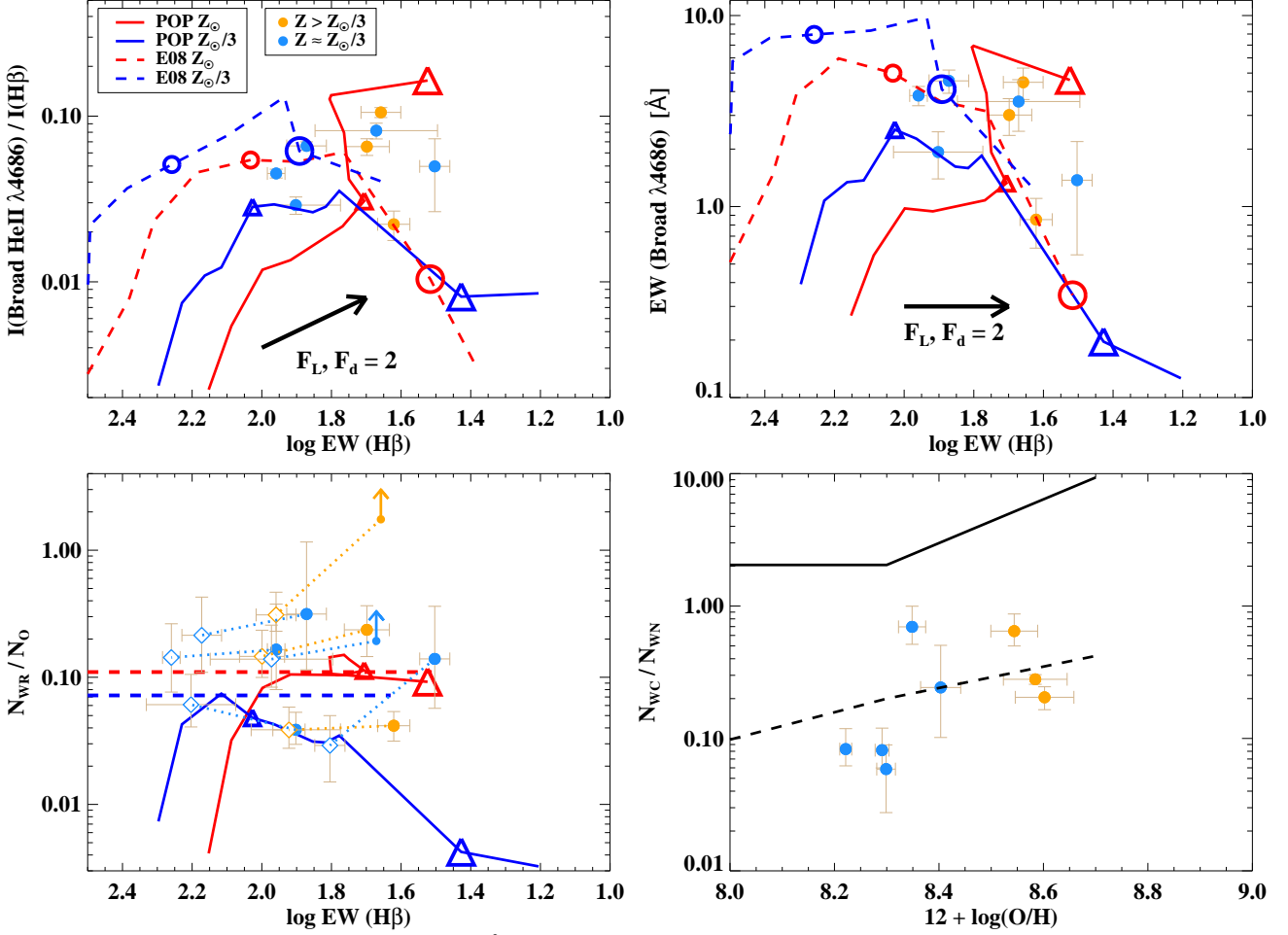


**Fig. 10: Top:** Intensity ratio of the He II 4686 Å broad line to H $\beta$  (left) and the EW of the broad line (right) vs. EW (H $\beta$ ), a good indicator of the age of young ionising populations. The data are coloured depending on their metallicity. Tracks from POPSTAR (solid line; simple population) and BPASS (dashed line; binary population) are displayed in different colours also depending on the metallicity. Open triangles mark the values for 4.5 (small triangles) and 5.5 Myr (large triangles), respectively, on the POPSTAR tracks. Open circles mark the values for 6 (small circles) and 12.5 Myr (large circles), respectively, on the BPASS tracks. The arrows labelled as  $F_L = 2$  and  $F_d = 2$  illustrate how the tracks would move on the plot if half of the ionising photons actually escape the ionised regions or are absorbed by dust grains within the H II region. **Bottom-left:** Derived ratio of the number of WRs over the number of O stars vs. EW (H $\beta$ ). Lower-limits are provided for R1 in NGC 3381 and NGC 3773. Open diamonds show how the data would move in the plot if half of the photons escaped or were absorbed (the dotted lines connect each case); here, the upper-limits disappear because having been the H $\beta$  flux increased, the derived number of O stars is not negative any more. The tracks from the BPASS models are completely horizontal because the only average values over the time of the WR phase are provided. **Bottom-right:** Ratio of the derived number of WC over WN stars vs. metallicity. Solid (dashed) line marks the track for the POPSTAR (BPASS) model.

in some age bins and practically highly non-linear in others) may vary almost nothing or dramatically, thus the variation of  $N_{\text{WR}}/N_{\text{O}}$  also ranges from almost nothing to a dramatic change. Those regions in which the ratio is higher than 0.2 cannot be reproduced at all with any kind of model if at least half of the ionising photons are missing by either process. Since the ratios in binary models are in general higher than those in simple models, the former are generally close to the observed ratios.

We could also compare the ratio of carbon to nitrogen WRs, namely  $N_{\text{WC}}/N_{\text{WN}}$ , with the predictions of models (Fig. 10, bottom-right), taking into account the high uncertainties involved specially when deriving  $N_{\text{WC}}$ . While simple models predict too high ratios, our derived values are closer to the predictions made by binary models. Yet, discrepancies with factors of  $\sim 2$  can be encountered. A similar agreement

is generally found at moderate and low metallicities when effects of rotation and binarity are included in the modelling (e.g., Neugent & Massey 2011; Neugent et al. 2012).

As a conclusion, we find that only in a few cases the observables can be reproduced by simple star models. In general, processes such as binarity, fast rotation, or even more complex processes (e.g. photon leakage, absorption by dust grains, IMF variations, etc.) are need to be included in the theoretical modelling of the stellar populations in order to better understand how massive stars evolve. This follows the recent line of discussion in observational studies of WR populations (e.g., Crowther 2007; B08a; López-Sánchez & Esteban 2010; Bibby & Crowther 2010, 2012; Kehrig et al. 2013).



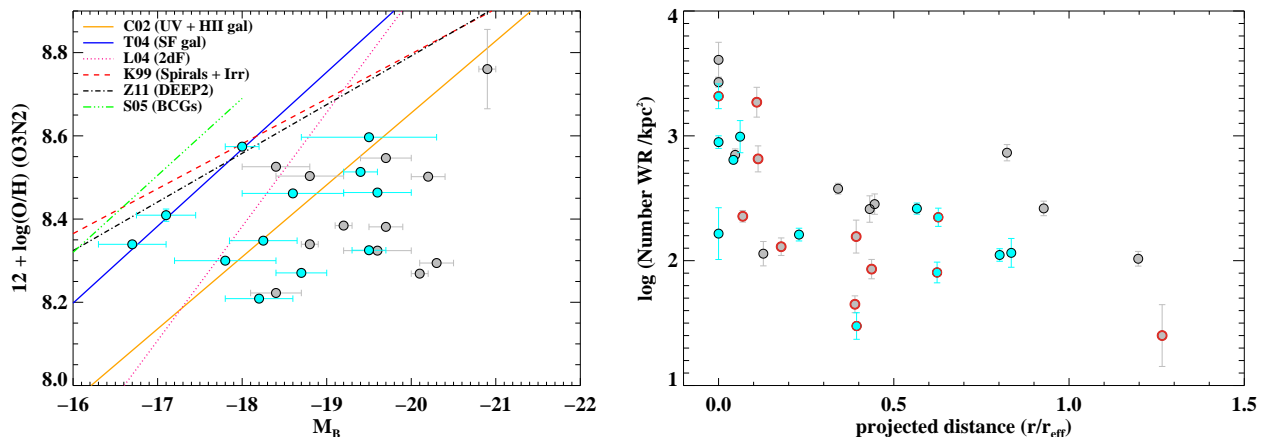


**Fig. 11: Left:** The luminosity-metallicity ( $L-Z$ ) relation of the galaxies in the CALIFA survey with detected WR stars, in grey those showing some signs of undergoing or recent interaction (M), and in blue those classified as isolated (I).  $L-Z$  relations for various galaxy samples from the literature are also drawn: UV-selected galaxies (solid orange; Contini et al. 2002), SDSS star-forming galaxies (solid blue; Tremonti et al. 2004), a large magnitude-limited sample (dotted pink; Lamareille et al. 2004), irregular and spiral galaxies (dashed red; Kobulnicky et al. 1999), emission-line galaxies at  $z \sim 0.8$  from the Deep Extragalactic Evolutionary Probe 2 survey (dotted-dashed; Zahid et al. 2011) and star-forming BCGs (three dotted-dashed green; Shi et al. (2005)). The large error bars in the absolute magnitudes refer to the uncertainties in the galaxy distance moduli, taken from NED. **Right:** number density of WRs vs. their projected galactocentric distance. The colours of the regions denote if they belong to a merging (M) or an isolated (I) galaxy. Regions circled in red are those whose host galaxy does not follow the luminosity-metallicity relation and have simultaneously a metallicity  $12 + \log(\text{O}/\text{H}) < 8.4$ .

#### 5.4. WRs and the environment: the GRB-WR connection

As mentioned in Sec. 4.1, 13 out of the 25 galaxies hosting WR regions show signs of interaction. Taking into account that young populations are also expected in normal spirals, irregulars and dwarf blue galaxies, this fact suggests that the number of WRs is particularly high in galaxy interactions. This is not entirely surprising, since merging processes are known to enhance the star formation activity in the galaxies involved (e.g. Kennicutt et al. 1987; Barton Gillespie et al. 2003; Geller et al. 2006; Di Matteo et al. 2008; Rodríguez Zaurín et al. 2010; Barrera-Ballesteros et al. 2015). This is also in agreement with studies of supernova radial distributions that found SNe Ibc (those associated with more massive stars and GRBs) more centrally concentrated in disturbed/interacting galaxies (Habergham et al. 2012).

Very few studies have focused on the issue of connecting the environment of the galaxy, the presence of WRs and the production of GRBs (e.g., Hammer et al. 2006; Han et al. 2010). MC14b investigated the environment of a single galaxy with strong presence WRs and tried to connect it with the properties of the hosts galaxies in Han et al. (2010), finding similarities in the integrated properties of GRB and WR hosts. A detailed study of the environment of local galaxies with similar properties to the GRB hosts is essential to better understand the physical properties of GRBs observed at moderate and high redshifts and the nature of their progenitors. The 25 galaxies with positive detection in this work allow us to dig deeper into this connection.

H10 performed a spectral analysis of 8 LGRB hosts in order to study the environment in which such energetic events can take place. Since, according to the core-collapse model, WRs are considered as the most favoured candidates to being the progenitors of LGRBs, the presence of WRs in their hosts provided evidence in favour. They identified some characteristics that support this connection. One of them is

that these galaxies do not follow the luminosity- and mass-metallicity relations obeyed typically by irregular, spiral and star-forming galaxies. The scenario of LGRBs occurring in host galaxies with *lower metallicities* than the general population is also supported by a few observational studies (e.g. Modjaz et al. 2011; Levesque et al. 2010a; Graham & Fruchter 2013). This under-abundance is naturally explained in galaxy mergers, since they induce radial gas mixing processes, such as inflows of external gas on to the central regions (e.g., Barnes & Hernquist 1996; Rupke et al. 2010).

We have explored in Fig. 11 (left) if our sample of host galaxies follow the luminosity-metallicity relation observed in the general population. We obtained the metallicity of the galaxies by integrating the whole spectrum within the CALIFA FoV and using the O3N2 calibration, as we did for the HII regions. For metallicities higher than about  $12 + \log(\text{O}/\text{H}) = 8.4$  the galaxies tend to follow the relation, although there are a couple of outliers. In contrast, galaxies with lower metallicities show a clear dichotomy: those with no clear signs of recent or current interaction processes (classified as isolated; I in Table 1) tend to follow the relation while those identified as merging (M in Table 1) are clearly outliers. Actually, even the most diverted object of the sample of isolated galaxies, UGC 10297, may present a disc truncation which could indicate a past minor merger (Comerón et al. 2012).

We have at least a sub-sample of about 10 galaxies, most of them undergoing an interaction, with similar characteristics to GRB hosts, namely moderate to low metallicity (Modjaz et al. 2011) and showing a significant offset in the luminosity-metallicity relation followed by the general galaxy population (Levesque et al. 2010b). But, are those hosts the ones that have larger number of WRs? Where are they located? Fig. 11 (right) shows a correlation between the number density of WRs (number of WRs/kpc<sup>2</sup>) and their projected distance to the centre of the galaxy. The Spearman's correlation coefficient is very

similar ( $\rho \sim -0.6$ ) in regions from both the isolated and merging galaxy sample, being somewhat stronger in the latter. While at distances shorter than about  $0.3 r_{\text{eff}}$  several hundreds and even thousands of WR are observed per  $\text{kpc}^2$ , in general an order of magnitude or less is observed at longer galactocentric distances.

The two regions with the highest number density are rather metal rich, and 2 regions out of 12 whose galaxies do not follow the luminosity-metallicity correlation have densities higher than  $1000 \text{ WRs/kpc}^2$ . We could assume that in those 12 regions the probability for a GRB to occur is higher. Therefore, the existence of more WRs would not necessarily guarantee more GRB events and they would not necessarily be in the very central regions (where larger number of WR are found). In fact, there are some studies that do not associate the presence of GRBs to that of WRs, at least not in the exact location of the WRs but at spatial shifts of about hundreds of pc away (Hammer et al. 2006; Christensen et al. 2008; Levesque et al. 2011; Thöne et al. 2014). Yet, the presence of WRs is found in the host galaxies. In those studies, the location of the GRBs does not lie necessarily in the central regions of the galaxy either (e.g., in Thöne et al. 2014 it is found about 7–8 kpc away). Although we have found galaxies with similar properties to the GRB hosts, more resolved studies of nearby GRB hosts are needed to better understand how these energetic phenomena occur and what is their relation with the WR population.

## 6. Conclusions

In this exploratory work, we have developed a technique to perform an automated search of Wolf-Rayet (WR) signatures through a pixel-by-pixel analysis of integral field spectroscopy (IFS) data of local galaxies. This procedure has been applied to a sample of 558 galaxies from the CALIFA survey plus the extended projects, spanning a wide range of physical properties. This represents the first systematic search of these peculiar populations in a large sample of galaxies observed with IFS, where we can have simultaneous spectral and spatial information. We present a catalogue of 44 regions with clear signatures of WR emission in the blue bump (five of them also showing the red bump), in 25 star-forming galaxies presenting a variety of morphologies (and environments): irregulars, blue dwarfs, spirals and interacting galaxies. We have performed a detailed analysis of the main properties of these regions, drawing the following conclusions:

1. We are able to detect WR emission in the spectrum of a pixel (with spatial scales spanning from 60 to about 600 pc) with equivalent widths (EW) of  $H\alpha$  typically higher than about  $15 \text{ \AA}$ . The detection of the red bump implies less contamination by underlying non-ionising populations, i.e.,  $\text{EW}(H\alpha) > 60 \text{ \AA}$ . For the candidate regions showing WR features, namely, WR regions, the distribution of EWs (ranging from 25 to  $700 \text{ \AA}$ ) peaks at  $125\text{--}160 \text{ \AA}$ , decreasing at larger values (i.e., younger ages). The presence of a turnover in this distribution is consistent with the WR phase starting a few Myr after the population is born.
2. While most of the regions are distributed within one effective radius, only a third of them are found at the centre of the galaxy, within  $\sim 1 \text{ kpc}$  or less from the nucleus. While most WR regions are found in  $H\alpha$  clumps (i.e.,  $H\text{II}$  regions or aggregates), several seem to be associated with the diffuse  $H\alpha$  emission in the central regions of the galaxy. The latter are probably associated to  $H\text{II}$  regions that are not

resolved and/or not distinguished due to the high  $H\alpha$  surface brightness in the centre of the galaxies.

3. We have performed a detailed fitting of the spectra of these regions considering the broad stellar and narrow nebular emission lines in the WR blue bump. Although large part of the emission is likely to be originated from late-type nitrogen WRs (WNL), direct positive detection from early-types (WNE) and carbon WRs (WC) has been obtained in 2 and 5 regions, respectively. Plausible evidence of a non-negligible percentage of early-type carbon WRs (WCEs) has been found in all regions. The WR regions host from dozens to more than 30,000 WRs, the latter in the two most distant galaxies. Actually, in one of the two (NGC 7469) a direct evidence has been found of the existence of strong star formation with large number of WRs and Seyfert activity within the central 2 kpc.
4. There is a strong presence of WRs in galaxy interactions, irregulars and blue dwarf galaxies, where strong star formation is observed. Galaxies showing signatures of recent past or undergoing merging processes have in general similar integrated properties to the hosts of gamma-ray burst events that also show an important presence of WR populations. However, the existence of a large number of WRs does not necessarily guarantee more GRB events or that they have to occur necessarily in the host very central regions. This is consistent with recent studies on GRB hosts.
5. We have discussed the effect of the dilution of the WR features when integrating the spectra at larger apertures than those where the feature is originally detected. These effects have to be taken into account when applying WR searching techniques that are currently widely used.
6. We have found clear evidence that the effects of binary stars and other processes (i.e., UV photon leakage, absorption by UV photons within the  $H\text{II}$  nebula) need to be taken into account in the stellar population modelling in order to better reproduce the observed fluxes of the WR stellar emission lines, equivalent widths and the ratios of WR to O stars as well as between WR sub-types, especially at moderate to low metallicities. If binarity is important, the WR phase could last up to 10 Myr or so. Although very low metallicity regimes are not explored in this study, our result is consistent with previous studies that claim that simple star models fail dramatically to reproduce many of the observed properties of these stars in the Local Universe in low metallicity environments.

## Acknowledgments

DMC, AID and FFRO would like to acknowledge financial support provided by the project AYA2010-21887-C04-03 (former *Ministerio de Ciencia e Innovación*, Spain) as well as the exchange programme “Study of Emission-Line Galaxies with Integral-Field Spectroscopy” (SELGIFS, FP7-PEOPLE-2013-IRSES-612701), funded by the EU through the IRSES scheme. AMI acknowledges support from Agence Nationale de la Recherche through the STILISM project (ANR-12-BS05-0016-02). RGD acknowledges support through the project AYA2014-57490-P. CJW acknowledges support through the Marie Curie Career Integration Grant 303912. This research has made use of the NASA/IPAC Extragalactic Database (NED) which is operated by the Jet Propulsion Laboratory, California Institute of Technology, under contract with the National Aeronautics and Space Administration. Support for LG is provided by the Ministry of Economy, Development, and Tourism’s Millennium

Science Initiative through grant IC120009, awarded to The Millennium Institute of Astrophysics, MAS. LG acknowledges support by CONICYT through FONDECYT grant 3140566.

## References

- Abbott, J. B., Crowther, P. A., Drissen, L., et al. 2004, *MNRAS*, 350, 552
- Allen, D. A., Wright, A. E., & Goss, W. M. 1976, *MNRAS*, 177, 91
- Alloin, D., Collin-Souffrin, S., Joly, M., & Vigroux, L. 1979, *A&A*, 78, 200
- Baldwin, J. A., Phillips, M. M., & Terlevich, R. 1981, *PASP*, 93, 5
- Barnes, J. E. & Hernquist, L. 1996, *ApJ*, 471, 115
- Barrera-Ballesteros, J. K., Sánchez, S. F., García-Lorenzo, B., et al. 2015, *A&A*, 579, A45
- Barton Gillespie, E., Geller, M. J., & Kenyon, S. J. 2003, *ApJ*, 582, 668
- Bibby, J. L. & Crowther, P. A. 2010, *MNRAS*, 405, 2737
- Bibby, J. L. & Crowther, P. A. 2012, *MNRAS*, 420, 3091
- Brinchmann, J., Kunth, D., & Durret, F. 2008a, *A&A*, 485, 657
- Brinchmann, J., Pettini, M., & Charlot, S. 2008b, *MNRAS*, 385, 769
- Cairós, L. M., Caon, N., Zurita, C., et al. 2010, *A&A*, 520, A90
- Cardelli, J. A., Clayton, G. C., & Mathis, J. S. 1989, *ApJ*, 345, 245
- Casasola, V., Hunt, L. K., Combes, F., et al. 2010, *A&A*, 510, A52
- Castellanos, M., Díaz, A. I., & Terlevich, E. 2002, *MNRAS*, 337, 540
- Cerviño, M. 1998, PhD thesis, UMC, Spain, (1998)
- Christensen, L., Vreeswijk, P. M., Sollerman, J., et al. 2008, *A&A*, 490, 45
- Cid Fernandes, R., Gu, Q., Melnick, J., et al. 2004, *MNRAS*, 355, 273
- Cid Fernandes, R., Mateus, A., Sodré, L., Stasińska, G., & Gomes, J. M. 2005, *MNRAS*, 358, 363
- Cid Fernandes, R., Stasińska, G., Mateus, A., & Vale Asari, N. 2011, *MNRAS*, 413, 1687
- Comerón, S., Elmegreen, B. G., Salo, H., et al. 2012, *ApJ*, 759, 98
- Conti, P. S. 1991, *ApJ*, 377, 115
- Conti, P. S. & Massey, P. 1989, *ApJ*, 337, 251
- Contini, T., Treyer, M. A., Sullivan, M., & Ellis, R. S. 2002, *MNRAS*, 330, 75
- Crowther, P. A. 2007, *ARA&A*, 45, 177
- Crowther, P. A. & Hadfield, L. J. 2006, *A&A*, 449, 711
- Crowther, P. A., Hadfield, L. J., Clark, J. S., Negueruela, I., & Vacca, W. D. 2006, *MNRAS*, 372, 1407
- Cutri, R. M., Rieke, G. H., Tokunaga, A. T., Willner, S. P., & Rudy, R. J. 1984, *ApJ*, 280, 521
- Dellenbusch, K. E., Gallagher, III, J. S., Knezek, P. M., & Noble, A. G. 2008, *AJ*, 135, 326
- Di Matteo, P., Bournaud, F., Martig, M., et al. 2008, *A&A*, 492, 31
- Drissen, L., Crowther, P. A., Ubeda, L., & Martin, P. 2008, *MNRAS*, 389, 1033
- Drissen, L., Moffat, A. F. J., & Shara, M. M. 1990, *ApJ*, 364, 496
- Drissen, L., Moffat, A. F. J., & Shara, M. M. 1993a, *AJ*, 105, 1400
- Drissen, L., Roy, J.-R., & Moffat, A. F. J. 1993b, *AJ*, 106, 1460
- Eldridge, J. J., Izzard, R. G., & Tout, C. A. 2008, *MNRAS*, 384, 1109
- Eldridge, J. J. & Stanway, E. R. 2009, *MNRAS*, 400, 1019
- Ercolano, B., Wesson, R., Zhang, Y., et al. 2004, *MNRAS*, 354, 558
- Falcón-Barroso, J., Sánchez-Blázquez, P., Vazdekis, A., et al. 2011, *A&A*, 532, A95
- Ferland, G. J., Korista, K. T., Verner, D. A., et al. 1998, *PASP*, 110, 761
- Fruchter, A. S., Levan, A. J., Strolger, L., et al. 2006, *Nature*, 441, 463
- Galama, T. J., Vreeswijk, P. M., van Paradijs, J., et al. 1998, *Nature*, 395, 670
- Galbany, L., Stanishev, V., Mourão, A. M., et al. 2014, *A&A*, 572, A38
- García-Benito, R., Díaz, A., Hägele, G. F., et al. 2010, *MNRAS*, 408, 2234
- García-Benito, R., Zibetti, S., Sánchez, S. F., et al. 2014, *ArXiv e-prints*
- García-Lorenzo, B., Marquez, I., Barrera-Ballesteros, J. K., et al. 2014, *ArXiv e-prints*
- Geller, M. J., Kenyon, S. J., Barton, E. J., Jarrett, T. H., & Kewley, L. J. 2006, *AJ*, 132, 2243
- Giuricin, G., Monaco, P., Madirossian, F., & Mezzetti, M. 1994, *ApJ*, 425, 450
- González Delgado, R. M., Cerviño, M., Martins, L. P., Leitherer, C., & Hauschildt, P. H. 2005, *MNRAS*, 357, 945
- González Delgado, R. M. & Pérez, E. 1997, *ApJS*, 108, 199
- Gonzalez-Delgado, R. M., Perez, E., Diaz, A. I., et al. 1995, *ApJ*, 439, 604
- Gonzalez-Delgado, R. M., Perez, E., Tenorio-Tagle, G., et al. 1994, *ApJ*, 437, 239
- Graham, J. F. & Fruchter, A. S. 2013, *ApJ*, 774, 119
- Gu, Q., Zhao, Y., Shi, L., Peng, Z., & Luo, X. 2006, *AJ*, 131, 806
- Guseva, N. G., Izotov, Y. I., & Thuan, T. X. 2000, *ApJ*, 531, 776
- Habergham, S. M., James, P. A., & Anderson, J. P. 2012, *MNRAS*, 424, 2841
- Hadfield, L. J. & Crowther, P. A. 2006, *MNRAS*, 368, 1822
- Hadfield, L. J. & Crowther, P. A. 2007, *MNRAS*, 381, 418
- Hadfield, L. J., Crowther, P. A., Schild, H., & Schmutz, W. 2005, *A&A*, 439, 265
- Hainich, R., Rühling, U., Todt, H., et al. 2014, *A&A*, 565, A27
- Hammer, F., Flores, H., Schaerer, D., et al. 2006, *A&A*, 454, 103
- Han, X. H., Hammer, F., Liang, Y. C., et al. 2010, *A&A*, 514, A24
- Heckman, T. M., Beckwith, S., Blitz, L., Skrutskie, M., & Wilson, A. S. 1986, *ApJ*, 305, 157
- Heckman, T. M., González-Delgado, R., Leitherer, C., et al. 1997, *ApJ*, 482, 114
- Hjorth, J., Sollerman, J., Møller, P., et al. 2003, *Nature*, 423, 847
- Ho, L. C., Filippenko, A. V., & Sargent, W. L. 1995, *ApJS*, 98, 477
- Hunt, L. K. & Hirashita, H. 2009, *A&A*, 507, 1327
- Husemann, B., Jahnke, K., Sánchez, S. F., et al. 2013, *A&A*, 549, A87
- Izotov, Y. I. & Thuan, T. X. 1998, *ApJ*, 500, 188
- Izotov, Y. I., Thuan, T. X., & Lipovetsky, V. A. 1997, *ApJS*, 108, 1
- James, B. L., Tsamis, Y. G., Barlow, M. J., et al. 2009, *MNRAS*, 398, 2
- Karthick, M. C., López-Sánchez, Á. R., Sahu, D. K., Sanwal, B. B., & Bisht, S. 2014, *MNRAS*, 439, 157
- Kauffmann, G., Heckman, T. M., Tremonti, C., et al. 2003, *MNRAS*, 346, 1055
- Kehrig, C., Pérez-Montero, E., Vílchez, J. M., et al. 2013, *MNRAS*, 432, 2731
- Kehrig, C., Vílchez, J. M., Sánchez, S. F., et al. 2008, *A&A*, 477, 813
- Kelly, P. L., Kirshner, R. P., & Pahre, M. 2008, *ApJ*, 687, 1201
- Kelz, A., Verheijen, M. A. W., Roth, M. M., et al. 2006, *PASP*, 118, 129
- Kennicutt, Jr., R. C. 1984, *ApJ*, 287, 116
- Kennicutt, Jr., R. C., Roettiger, K. A., Keel, W. C., van der Hulst, J. M., & Hummel, E. 1987, *AJ*, 93, 1011
- Kewley, L. J., Dopita, M. A., Sutherland, R. S., Heisler, C. A., & Trevena, J. 2001, *ApJ*, 556, 121
- Kiminki, D. C. & Kobulnicky, H. A. 2012, *ApJ*, 751, 4
- Kobulnicky, H. A. & Fryer, C. L. 2007, *ApJ*, 670, 747
- Kobulnicky, H. A. & Zaritsky, D. 1999, *ApJ*, 511, 118
- Kudritzki, R. P. 2002, *ApJ*, 577, 389
- Kunth, D. & Joubert, M. 1985, *A&A*, 142, 411
- Kunth, D. & Sargent, W. L. W. 1981, *A&A*, 101, L5
- Kunth, D. & Sargent, W. L. W. 1983, *ApJ*, 273, 81
- Lamareille, F., Mouhcine, M., Contini, T., Lewis, I., & Maddox, S. 2004, *MNRAS*, 350, 396
- Leoudas, G., Sollerman, J., Levan, A. J., et al. 2010, *A&A*, 518, A29
- Levesque, E. M., Berger, E., Kewley, L. J., & Bagley, M. M. 2010a, *AJ*, 139, 694
- Levesque, E. M., Berger, E., Soderberg, A. M., & Chornock, R. 2011, *ApJ*, 739, 23
- Levesque, E. M., Kewley, L. J., Berger, E., & Zahid, H. J. 2010b, *AJ*, 140, 1557
- Lopez, L. A., Krumholz, M. R., Bolatto, A. D., Prochaska, J. X., & Ramirez-Ruiz, E. 2011, *ApJ*, 731, 91
- López-Sánchez, Á. R. 2010, *A&A*, 521, A63
- López-Sánchez, Á. R., Dopita, M. A., Kewley, L. J., et al. 2012, *MNRAS*, 426, 2630
- López-Sánchez, Á. R. & Esteban, C. 2010, *A&A*, 516, A104
- López-Sánchez, Á. R., Mesa-Delgado, A., López-Martín, L., & Esteban, C. 2011, *MNRAS*, 411, 2076
- Marino, R. A., Rosales-Ortega, F. F., Sánchez, S. F., et al. 2013, *A&A*, 559, A114
- Martín-Manjón, M. L., García-Vargas, M. L., Mollá, M., & Díaz, A. I. 2010, *MNRAS*, 403, 2012
- Massey, P. 2003, *ARA&A*, 41, 15
- Massey, P., Bresolin, F., Kudritzki, R. P., Puls, J., & Pauldrach, A. W. A. 2004, *ApJ*, 608, 1001
- Massey, P. & Hunter, D. A. 1998, *ApJ*, 493, 180
- Meynet, G. 1995, *A&A*, 298, 767
- Meynet, G. & Maeder, A. 2005, *A&A*, 429, 581
- Miller, B. W. & Rudie, G. 2008, in *IAU Symposium*, Vol. 245, *IAU Symposium*, ed. M. Bureau, E. Athanassoula, & B. Barbuy, 311–312
- Miralles-Caballero, D., Colina, L., Arribas, S., & Duc, P.-A. 2011, *AJ*, 142, 79
- Miralles-Caballero, D., Díaz, A. I., Rosales-Ortega, F. F., Pérez-Montero, E., & Sánchez, S. F. 2014a, *MNRAS*, 440, 2265
- Miralles-Caballero, D., Rosales-Ortega, F. F., Díaz, A. I., et al. 2014b, *MNRAS*, 445, 3803
- Modjaz, M., Kewley, L., Bloom, J. S., et al. 2011, *ApJ*, 731, L4
- Modjaz, M., Stanek, K. Z., Garnavich, P. M., et al. 2006, *ApJ*, 645, L21
- Mollá, M., García-Vargas, M. L., & Bressan, A. 2009, *MNRAS*, 398, 451
- Monreal-Ibero, A., Vílchez, J. M., Walsh, J. R., & Muñoz-Tuñón, C. 2010, *A&A*, 517, A27+
- Monreal-Ibero, A., Walsh, J. R., & Vílchez, J. M. 2012, *A&A*, 544, A60
- Monreal-Ibero, A., Walsh, J. R., Westmoquette, M. S., & Vílchez, J. M. 2013, *A&A*, 553, A57
- Neugent, K. F. & Massey, P. 2011, *ApJ*, 733, 123
- Neugent, K. F., Massey, P., & Georgy, C. 2012, *ApJ*, 759, 11
- Osterbrock, D. E. 1978, *Proceedings of the National Academy of Science*, 75, 540
- Osterbrock, D. E. 1989, *Astrophysics of gaseous nebulae and active galactic nuclei*, ed. Osterbrock, D. E.
- Osterbrock, D. E. & Cohen, R. D. 1982, *ApJ*, 261, 64
- Pérez-Montero, E. & Díaz, A. I. 2007, *MNRAS*, 377, 1195
- Pérez-Montero, E., García-Benito, R., Hägele, G. F., & Díaz, Á. I. 2010, *MNRAS*, 404, 2037
- Perez-Montero, E., Kehrig, C., Brinchmann, J., et al. 2013, *ArXiv e-prints*



- Pilyugin, L. S., Grebel, E. K., & Mattsson, L. 2012, MNRAS, 424, 2316
- Plauchu-Frayn, I., Del Olmo, A., Coziol, R., & Torres-Papaqui, J. P. 2012, A&A, 546, A48
- Rodríguez Zaurín, J., Tadhunter, C. N., & González Delgado, R. M. 2010, MNRAS, 403, 1317
- Rosales-Ortega, F. F., Kennicutt, R. C., Sánchez, S. F., et al. 2010, MNRAS, 405, 735
- Roth, M. M., Kelz, A., Fechner, T., et al. 2005, PASP, 117, 620
- Rupke, D. S. N., Kewley, L. J., & Barnes, J. E. 2010, ApJ, 710, L156
- Sana, H., de Mink, S. E., de Koter, A., et al. 2012, Science, 337, 444
- Sánchez, S. F., Kennicutt, R. C., Gil de Paz, A., et al. 2012a, A&A, 538, A8
- Sánchez, S. F., Rosales-Ortega, F. F., Iglesias-Páramo, J., et al. 2014, A&A, 563, A49
- Sánchez, S. F., Rosales-Ortega, F. F., Marino, R. A., et al. 2012b, A&A, 546, A2
- Sánchez-Portal, M., Díaz, Á. I., Terlevich, R., et al. 2000, MNRAS, 312, 2
- Sander, A., Todt, H., Hainich, R., & Hamann, W.-R. 2014, A&A, 563, A89
- Sargent, W. L. W. & Filippenko, A. V. 1991, AJ, 102, 107
- Schaerer, D., Contini, T., & Kunth, D. 1999, A&A, 341, 399
- Schaerer, D. & Vacca, W. D. 1998, ApJ, 497, 618
- Schild, H., Crowther, P. A., Abbott, J. B., & Schmutz, W. 2003, A&A, 397, 859
- Shara, M. M., Bibby, J. L., Zurek, D., et al. 2013, AJ, 146, 162
- Shi, F., Kong, X., Li, C., & Cheng, F. Z. 2005, A&A, 437, 849
- Shirazi, M. & Brinchmann, J. 2012, MNRAS, 421, 1043
- Sidoli, F., Smith, L. J., & Crowther, P. A. 2006, MNRAS, 370, 799
- Smith, L. F., Shara, M. M., & Moffat, A. F. J. 1990, ApJ, 348, 471
- Smith, L. J. & Willis, A. J. 1982, MNRAS, 201, 451
- Stanek, K. Z., Matheson, T., Garnavich, P. M., et al. 2003, ApJ, 591, L17
- Thöne, C. C., Christensen, L., Prochaska, J. X., et al. 2014, MNRAS, 441, 2034
- Tremonti, C. A., Heckman, T. M., Kauffmann, G., et al. 2004, ApJ, 613, 898
- Tresse, L., Maddox, S., Loveday, J., & Singleton, C. 1999, MNRAS, 310, 262
- Úbeda, L. & Drissen, L. 2009, MNRAS, 394, 1847
- Vacca, W. D. 1994, ApJ, 421, 140
- Vacca, W. D. & Conti, P. S. 1992, ApJ, 401, 543
- Van Bever, J. & Vanbeveren, D. 2003, A&A, 400, 63
- van Bever, J. & Vanbeveren, D. 2007, in Astronomical Society of the Pacific Conference Series, Vol. 367, Massive Stars in Interactive Binaries, ed. N. St.-Louis & A. F. J. Moffat, 579
- van der Hucht, K. A. 2001, VizieR Online Data Catalog, 3215, 0
- Vazdekis, A., Sánchez-Blázquez, P., Falcón-Barroso, J., et al. 2010, MNRAS, 404, 1639
- Walcher, C. J., Wisotzki, L., Bekeraité, S., et al. 2014, A&A, 569, A1
- Westmoquette, M. S., James, B., Monreal-Ibero, A., & Walsh, J. R. 2013, A&A, 550, A88
- Wilson, A. S., Baldwin, J. A., Sun, S.-D., & Wright, A. E. 1986, ApJ, 310, 121
- Woosley, S. E. & Heger, A. 2006, ApJ, 637, 914
- Youngblood, A. J. & Hunter, D. A. 1999, ApJ, 519, 55
- Zahid, H. J., Kewley, L. J., & Bresolin, F. 2011, ApJ, 730, 137

<sup>1</sup> Departamento de Física Teórica, Universidad Autónoma de Madrid, 28049 Madrid, Spain.

<sup>2</sup> Australian Astronomical Observatory, PO Box 915, North Ryde, NSW 1670, Australia.

<sup>3</sup> Department of Physics and Astronomy, Macquarie University, NSW 2109, Australia.

<sup>4</sup> Instituto Nacional de Astrofísica, Óptica y Electrónica, Luis E. Erro 1, 72840 Tonantzintla, Puebla, Mexico.

<sup>5</sup> GEPI, Observatoire de Paris, CNRS, Université Paris-Diderot, Place Jules Janssen, 92190 Meudon, France.

<sup>6</sup> Instituto de Astrofísica de Andalucía (CSIC), Glorieta de la Astronomía s/n, Aptdo. 3004, E18080-Granada, Spain.

<sup>7</sup> Instituto de Astronomía, Universidad Nacional Autónoma de México, A.P. 70-264, 04510, México, D.F.

<sup>8</sup> Leibniz-Institut für Astrophysik Potsdam (AIP), An der Sternwarte 16, D-14482 Potsdam, Germany.

<sup>9</sup> Millennium Institute of Astrophysics MAS, Nuncio Monseñor Sótero Sanz 100, Providencia, 7500011 Santiago, Chile.

<sup>10</sup> Departamento de Astronomía, Universidad de Chile, Camino El Observatorio 1515, Las Condes, Santiago, Chile.

<sup>11</sup> Max Planck Institute for Astronomy, Königstuhl 17, 69117 Heidelberg, Germany.

<sup>12</sup> Instituto de Astrofísica de Canarias (IAC), E-38205 La Laguna, Tenerife, Spain

<sup>13</sup> Centro de Astrofísica and Faculdade de Ciências, Universidade do Porto, Rua das Estrelas, 4150-762 Porto, Portugal.

<sup>14</sup> Centro Astronómico Hispano Alemán, Calar Alto, (CSIC-MPG), C/Jesús Durbán Remón 2-2, E-04004 Almería, Spain.

## Appendix A: Additional figures

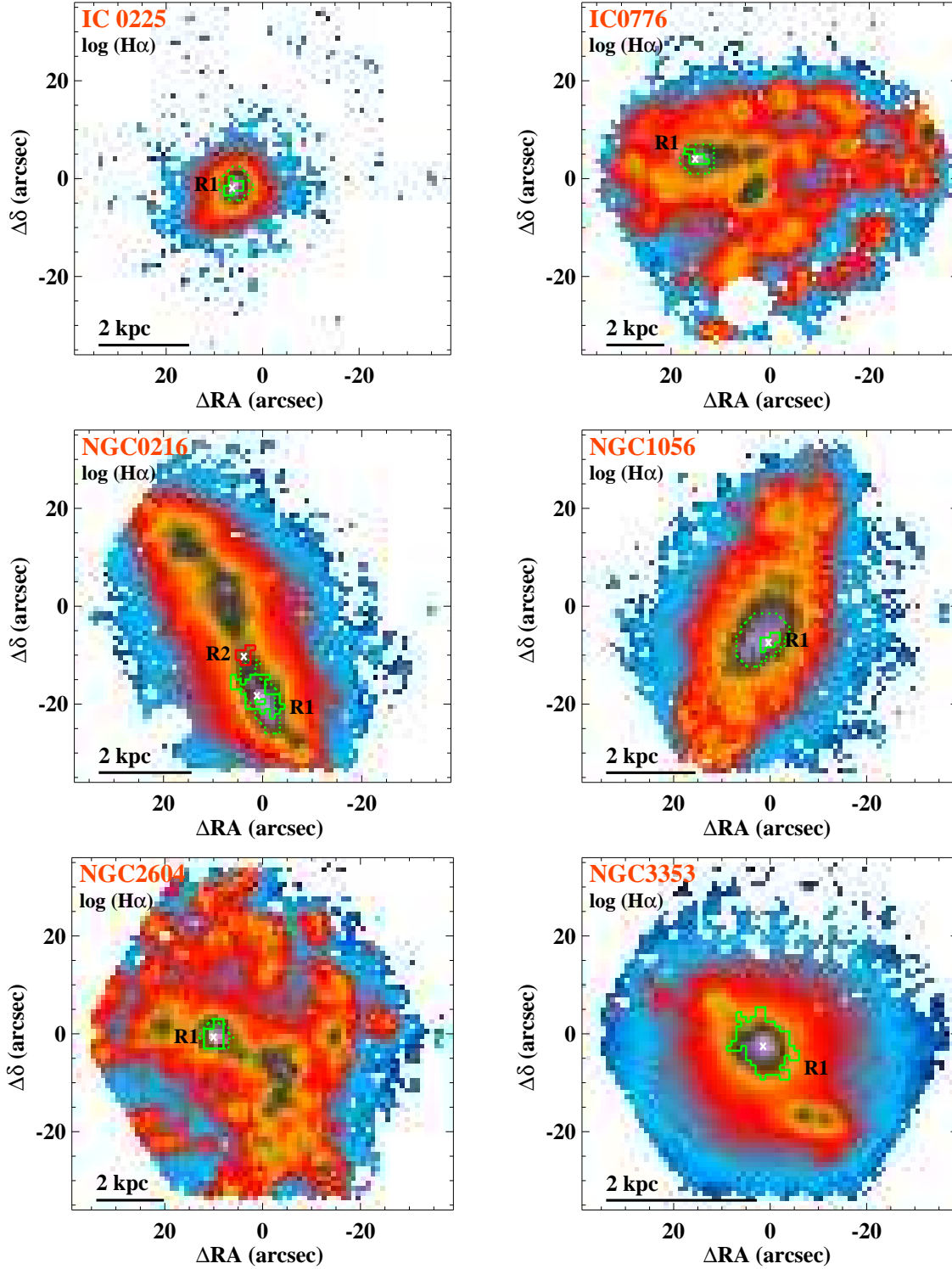


**Fig. A.1:** H $\alpha$  maps with logarithmic intensity scale of the galaxies with detected WR emission within the labelled regions enclosed by the green and red continuum contours. The pointed contours correspond to the associated H $\alpha$  clump identified using HIIEXPLORER, whenever the emission of the H $\alpha$  clump is more extended than that of the WR region. A cross indicates the barycenter of the region. The scale corresponding to 2 kpc is drawn at the bottom-left corner. North points up and East to the left.

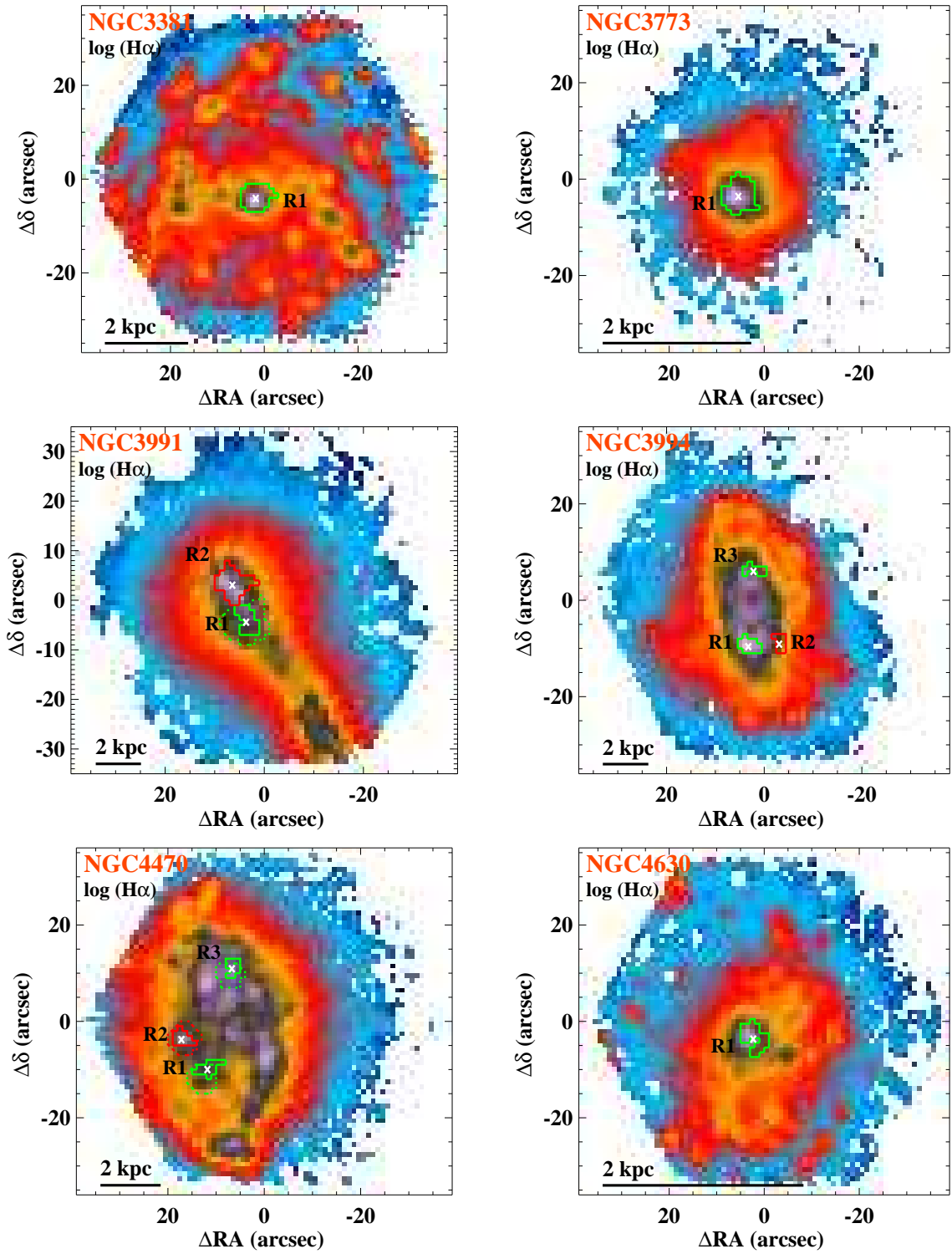


Fig. A.1: – Continued

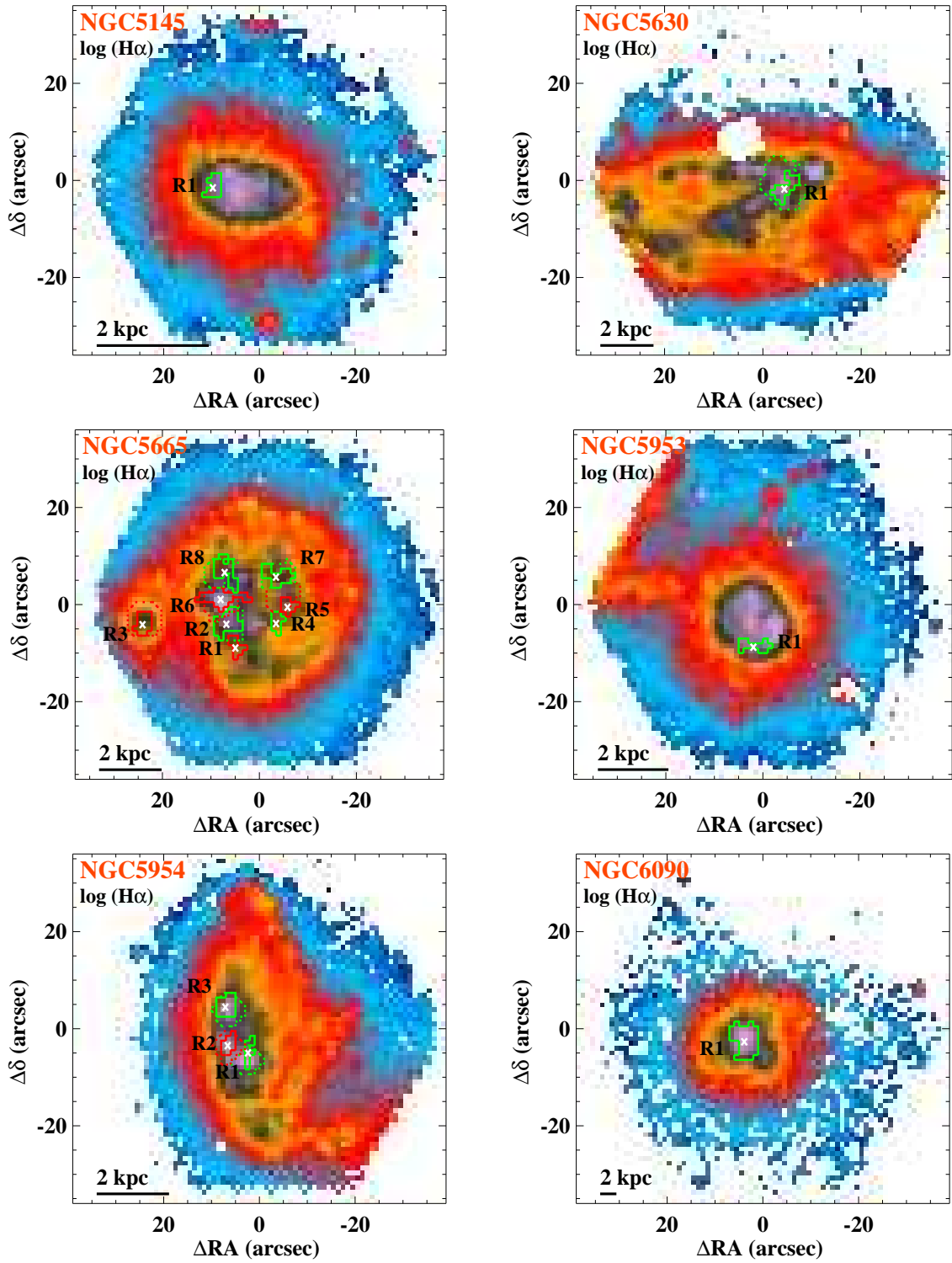


Fig. A.1: – Continued



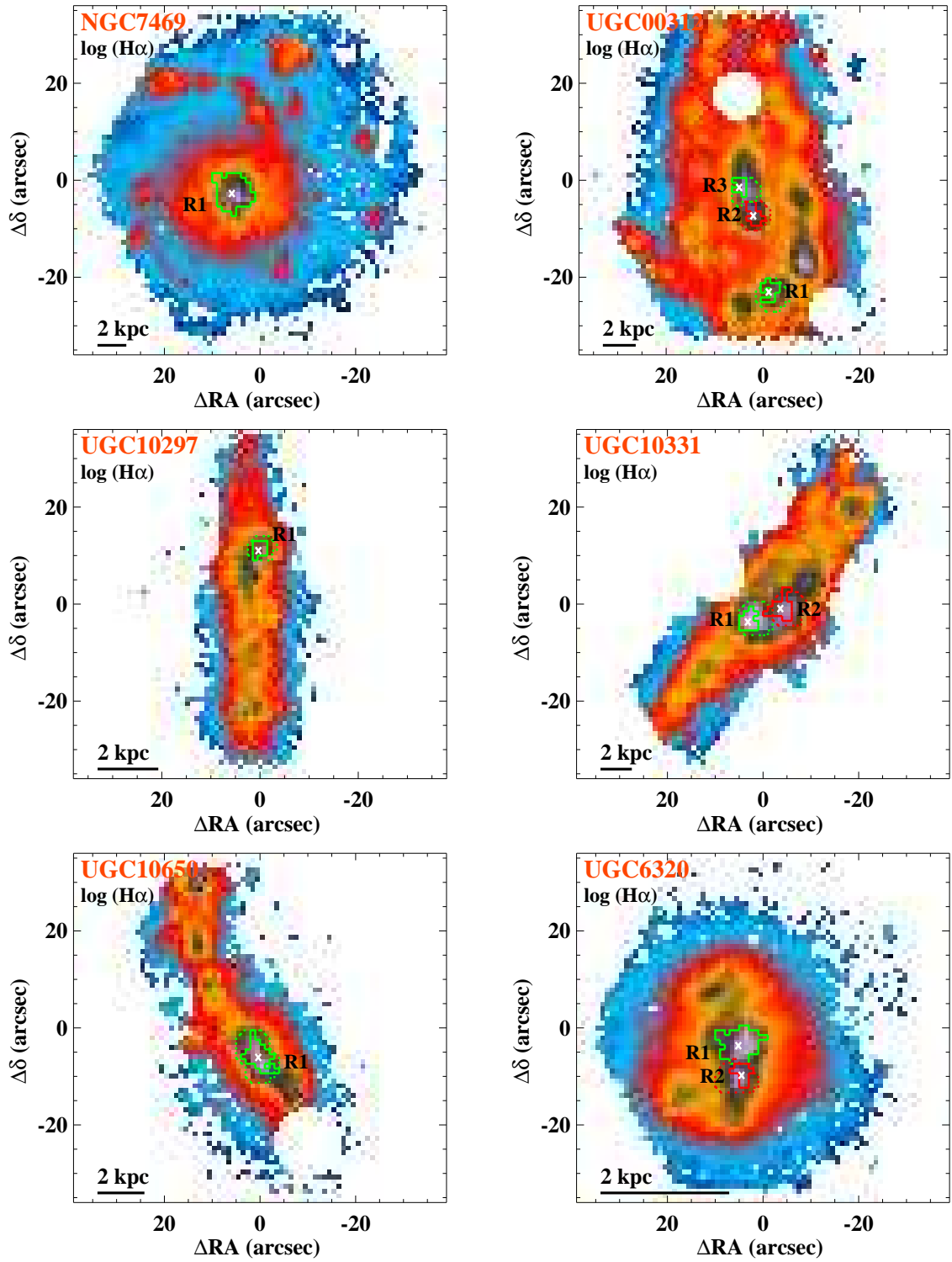


Fig. A.1: – Continued

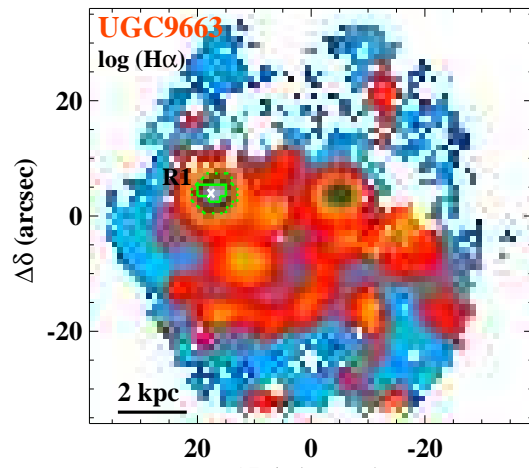
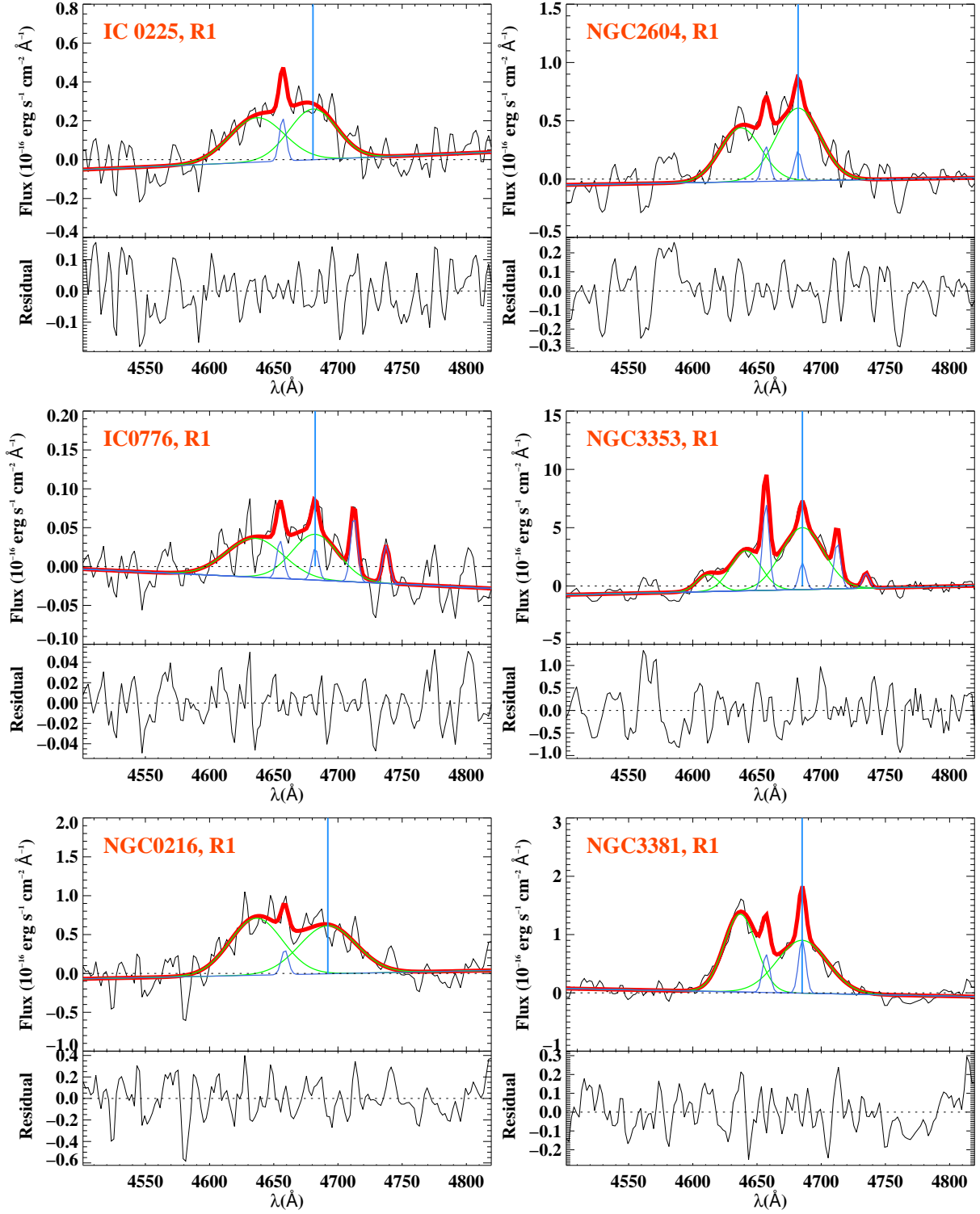


Fig. A.1: – Continued





**Fig. A.2:** Multiple-line fit of WR features within the blue bump. An almost horizontal blue line denotes the resulting continuum of the fit. The total fitted continuum plus emission lines to the blue bump is drawn by a thick-red line. The nebular (blue) and broad stellar (green) components of the fit are also drawn. The vertical blue line indicate the position of the He II 4686 Å line. In each case, an auxiliary plot shows in black the residuals (in flux units) after modelling all the stellar and nebular features. For the case of NGC 7469, the fitting has been done on the observed spectrum, as explained in the text.



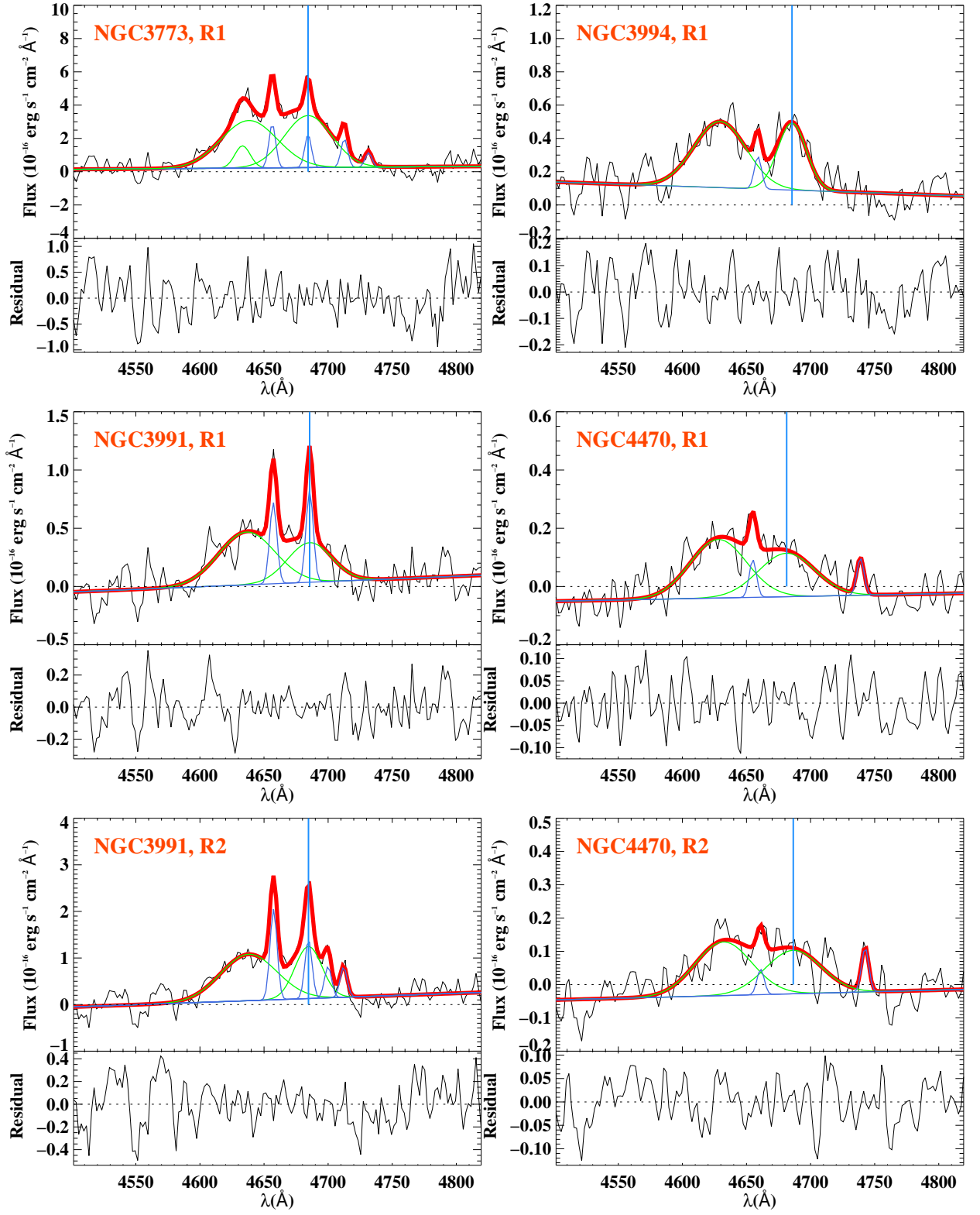


Fig. A.2: – Continued

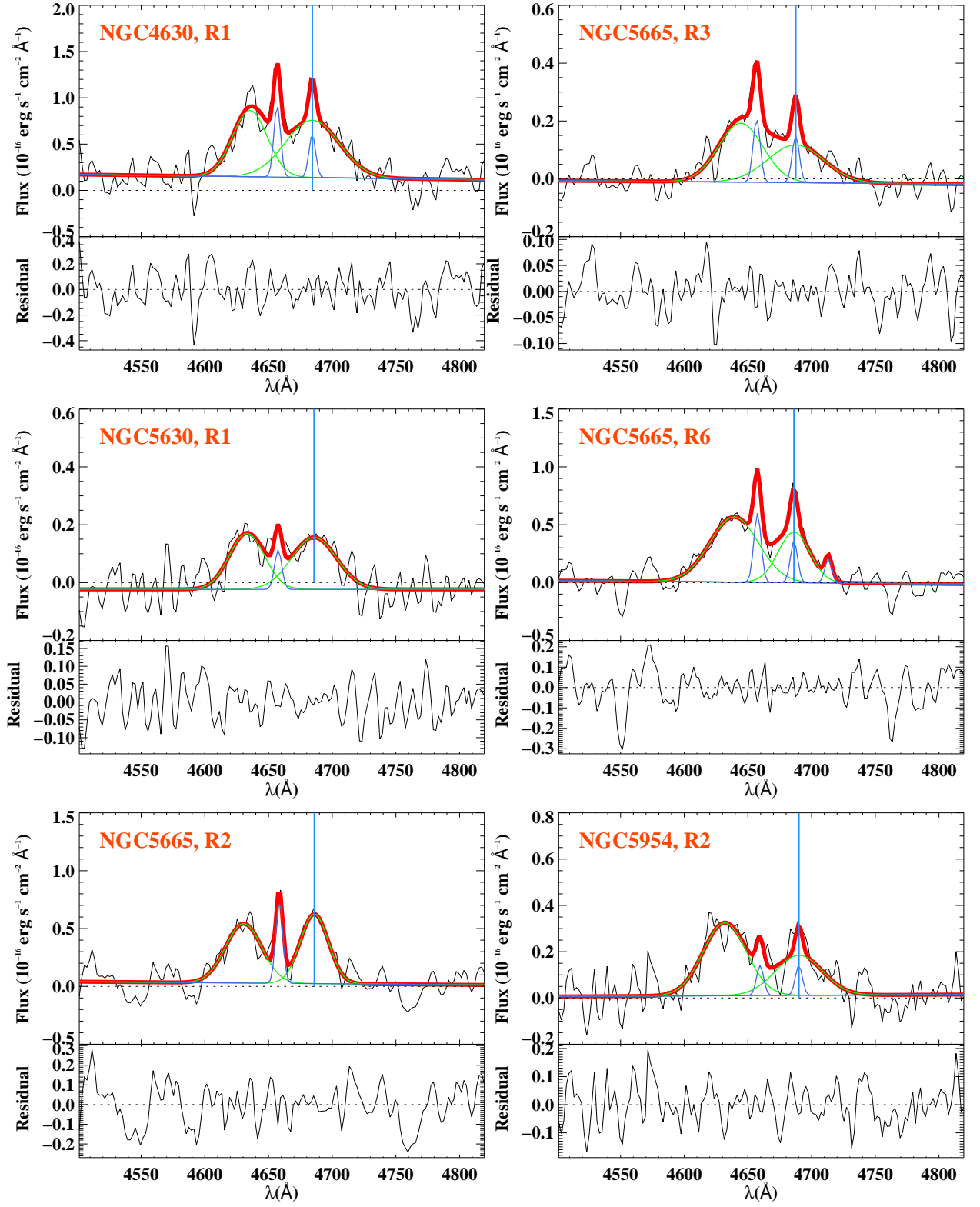


Fig. A.2: – Continued

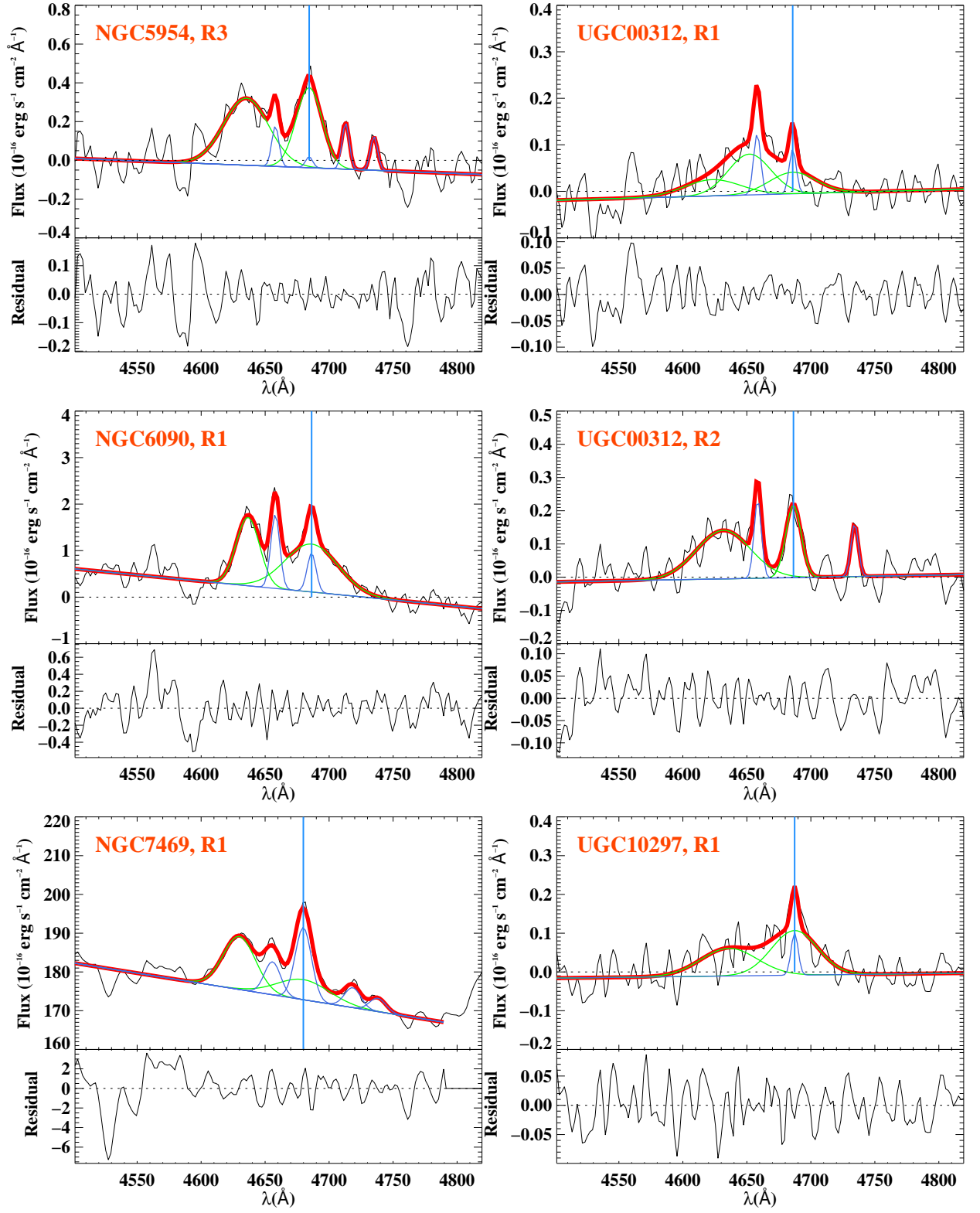


Fig. A.2: – Continued



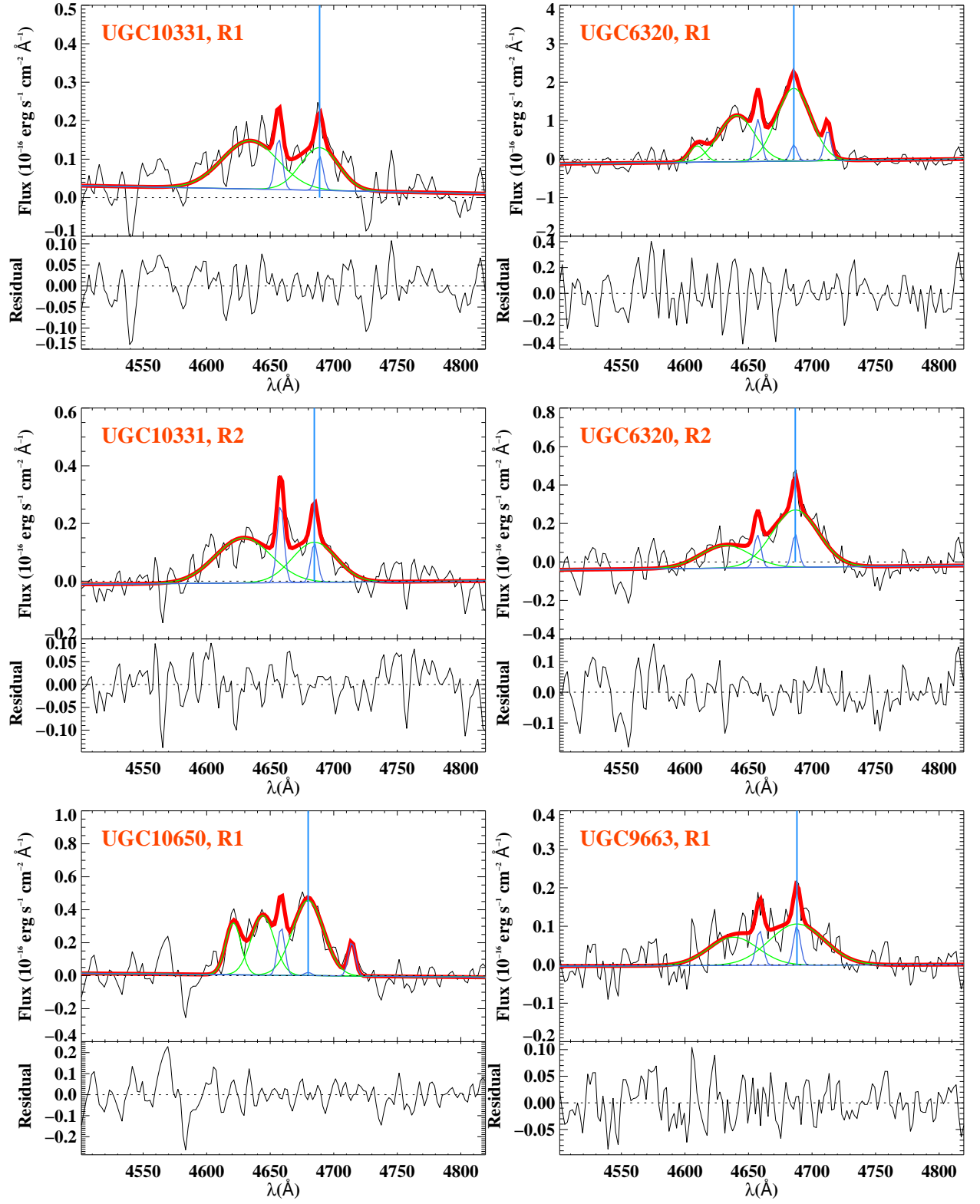
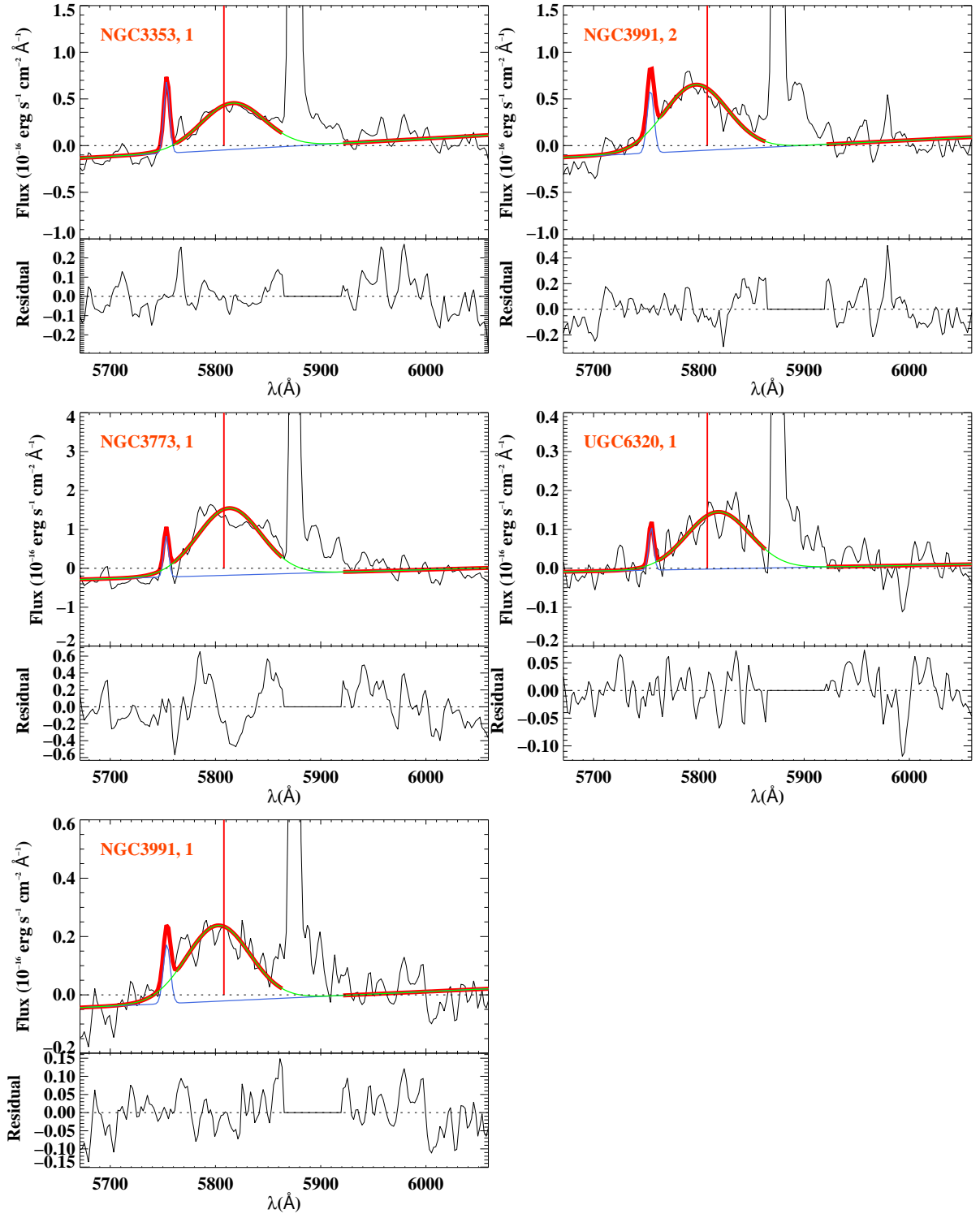


Fig. A.2: – Continued



**Fig. A.3:** Multiple-line fit of WR features within the red bump. In each figure the *residual* spectrum is shown in black. This corresponds to the emission gaseous and stellar line spectrum minus the modelled feature, in flux units. An almost horizontal blue line denotes the resulting continuum of the fit. The total fitted continuum plus emission lines to the blue bump is drawn by a thick-red line. The fit to the auroral [N II] 5755 Å line (blue) and broad stellar C iv 5808 Å feature (green) components of the fit are also drawn. The vertical red line indicate the position of the C iv 5808 Å feature.